공학박사 학위논문

Optimization of process parameters in piezo- and electrohydrodynamic inkjet printing

압전 방식과 전기수력학적 방식에 의한 잉크젯 프린팅 공정의 공정조건 최적화에 대한 연구

2013년 8월

서울대학교 대학원

화학생물공학부

이 아 영

Abstract

Optimization of process parameters in piezo- and electrohydrodynamic inkjet printing

Ayoung Lee

School of Chemical and Biological Engineering

The Graduate School

Seoul National University

Stable drop jettability is mandatory for a successful, technical scale inkjet printing, and accordingly, this aspect has attracted much attention in fundamental and applied research. In piezo inkjet printing (PIJ), drops are ejected by reverse piezo-electric effect. Previous studies were mainly focused on Newtonian fluids or polymer solutions. Here, we have investigated the drop jetting for zinc oxide (ZnO) particulate suspensions. Generally, the inverse Ohnesorge number $Z = Oh^{-1}$, which relates viscous

forces to inertia and surface tension, is sufficient to predict the jettability of single phase fluids. For the inkjet printer setup used here, jetting was possible for Newtonian fluids with $2.5 < Z < 26$, but in the identical Z-range, nonjetting and nozzle clogging occurred for certain suspensions. A so-called ring-slit device, which allows for simultaneous formation and detection of aggregates in strongly converging flow fields, and single particle detecting techniques, which allow for an accurate determination of the number and size of micrometer-sized aggregates in suspensions of nanoparticles, were used to study this phenomenon. Nozzle clogging is induced by heterocoagulation of micrometer-sized aggregates and ZnO nanoparticles in the elongational flow field at the nozzle exit. Clogging may occur even if the size of these aggregates is well below the nozzle diameter and their concentration is on the order of only a few hundred parts per million (ppm). Accordingly, increased colloidal stability of nanoparticles and reduced aggregate concentration result in better drop jettability. Also, a nozzle design resulting in a shorter exposure time of the ink to elongational flow and an increased flow velocity helps to avoid nozzle clogging.

In electrohydrodynamic (EHD) inkjet printing where droplet/jet is generated by electrostatic force, physical as well as electrical properties of the fluid should be taken into account to achieve desired performance. In this

study, a systematic approach was suggested to find the processing windows of EHD inkjet printing. Six dimensionless parameters were organized and applied to the printing system of ethanol/terpineol mixtures. Based on the correlation of dimensionless voltage and charge relaxation length, the jet diameter of cone-jet mode was characterized, and the semi-cone angle was compared with the theoretical Taylor angle. In addition, the ratio of electric normal force and electric tangential force on the charged surface of Taylor cone was recommended as a parameter judging the degree of cone-jet stability. The smaller the ratio, the more stable the cone-jet was. This approach was systematic and effective to obtain Taylor cone of cone-jet mode and to evaluate the jetting stability. The control of inks with optimized experimental parameters by this method will improve the jetting performance in EHD inkjet printing.

This study is expected to present processing protocols for designing experiments in piezo- and electrohydrodynamic inkjet printing by understanding the processing characteristics and issues, and contribute to the progress of inkjet technology to produce on-demand droplet/jet.

Keywords: Piezo inkjet printing, inverse Ohnesorge number $Z = Oh^{-1}$, ring-slit device, nozzle clogging, flow-induced aggregation, electrohydrodynamic inkjet printing, dimensionless parameters, cone-jet, jetting stability

Student Number: 2006-23219

Contents

List of Figures

List of Tables

Chapter 1. Introduction

1.1 Background on jetting behavior

Inkjet printing is an important direct patterning process for micro/nanofabrications of components such as polymerelectronics [Lewis *et al*. (2006), Jeoug *et al*. (2008), Sirringhaus *et al*. (2000), Kim *et al*. (2009)], field effect transistor (FET) [Bubel *et al*. (2009), Dasgupta *et al*. (2008), Mathews *et al*. (2010), Mechau *et al*. (2010), Okamura *et al*. (2008, 2010), Sun and Rogers (2007)], or solar cells [Habas *et al*. 2010] (Fig. 1-1). For a successful patterning, the ink formulation should be well designed not only for drop jettability and uniform deposition but also for electrical performance of the printed structure after drying. As for drop jettability, the dynamics of a colloidal suspension jet is known to be different from that of a Newtonian liquid in terms of nonstraight flying trajectories and nonaxisymmetric ligaments [Wang *et al*. (2012)]. The poor jetting behavior brings out difficulties and irregularities in the printing process. In spreading and leveling [Tsai *et al*. (2010), Maki and Kumar (2011)], Marangoni flow, which is caused by concentration gradient and particle adsorption to the

liquid−air interface, and non-Newtonian flow behavior influence the leveling process and may sometimes cause the so-called coffee ring effect. Drying conditions and especially the time scale of drying control the microstructure of the printed film, in particular its porosity and particle ordering [Cardinal *et al.* (2010)]. Nevertheless, due to the complexities not only of the printing process, which include both shear and strong elongational flow fields at high fluid velocities, but also of the ink composition itself, characterizing and analyzing the jetting phenomena under strong flow fields are very important and challenging.

1.2 Drop-on-demand piezo inkjet printing (PIJ)

Many factors affect the performance of drop-on-demand piezo inkjet printing (PIJ). They include processing parameters [Cibis and Krüger (2007), Kwon and Kim (2007, 2009)] such as driving voltage (pulse height), dwell time (pulse width), and repetition rate, as well as fluid properties [Perelaer *et al*. (2009), Jang *et al*. (2009), Jo *et al*. (2009)] such as surface tension σ, viscosity η, and density ρ. For Newtonian fluids, drop formation is determined by the dimensionless number, $Z = (d\rho\sigma)^{1/2}/\eta$, where d is the nozzle diameter, which is the characteristic length scale of the printing head. Z is often called inverse Ohnesorge number Oh^{-1} and is related to the Reynolds (Re) and Weber (We) numbers, $Z = Oh^{-1} = Re/We^{1/2}$. If Z is too low, no droplet can be formed, and if Z is too high, the formation of satellite droplets results in poor printing quality. Tai *et al*. (2008) observed drop ejection in the range of $0.67 < Z < 50$ for aqueous mixtures of varying glycerol compositions (0−80 wt %) with nozzle diameter d = 50 μm.

The printing quality can be improved by adding a small amount of a high molecular weight polymer. It means that even when two inks are in similar range of Z the jettability can be changed by polymer addition suppressing the formation of satellite droplets. To reflect the feature of this

kind, additional rheological parameters need to be considered. For polymer solutions, the complex shear modulus $G^* = G' + iG''$ or the extensional viscosity may be used, and since inkjet printing is a fast process the storage and loss moduli, G' and G'' at high frequency may be most relevant [Tai *et al*. (2008), Tuladhar and Mackley (2008), Vadillo *et al*. (2010a, 2010b)]. The viscoelastic properties of polystyrene fluids using piezo axial vibrator (PAV) at high frequency are in Fig. 1-2.

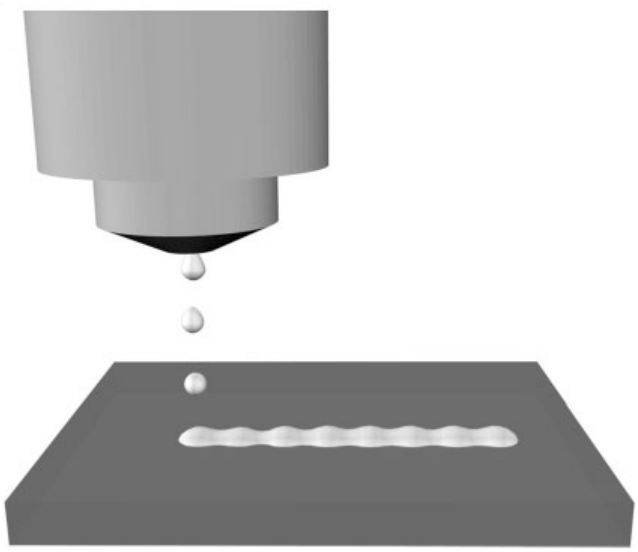

Fig. 1-1 Drop jetting behavior in piezo inkjet printing [Lewis *et al*. (2006)].

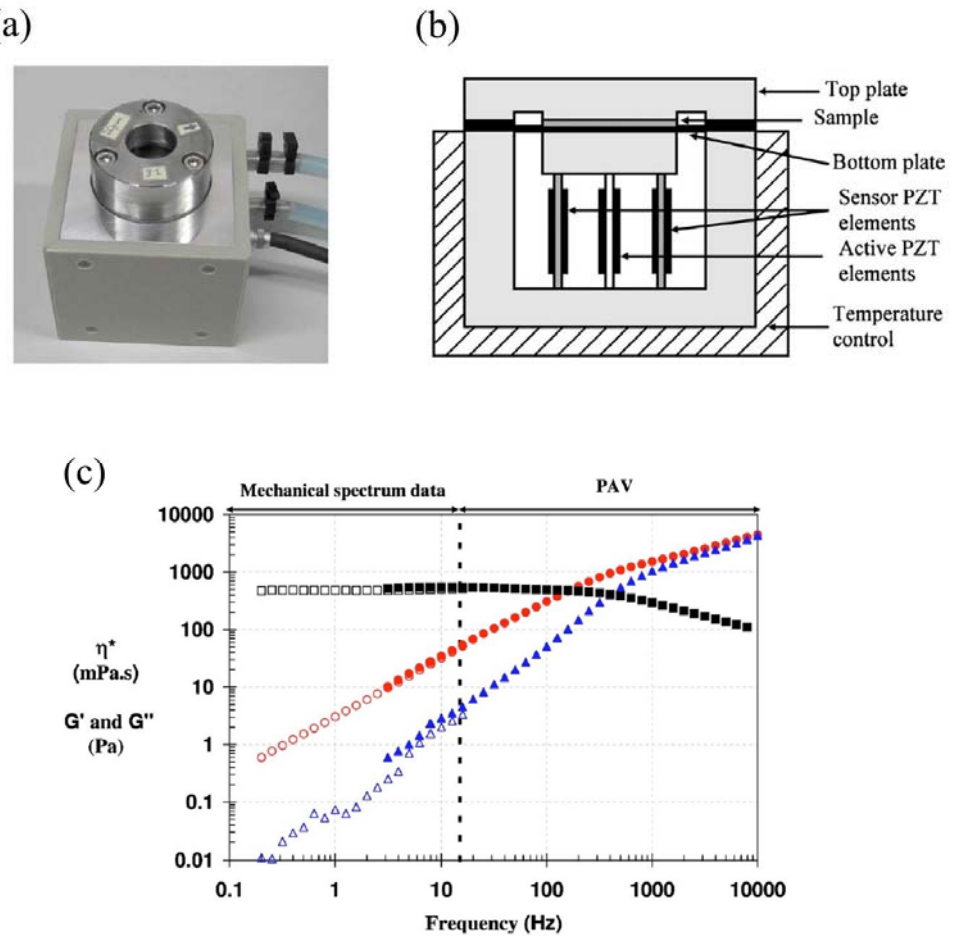

Fig. 1-2 (a) PAV device, (b) schematic of PAV, and (c) viscoelastic properties for DEP-10 wt% of monodisperse polystyrene 210 kg/mol [Vadillo *et al.* (2010b)].

For particulate inks including metallic or semiconducting nanoparticles, dispersion stability should be controlled since small particles tend to aggregate, which eventually affects printing quality. Surfactants or polymeric additives adsorbing on the particle surface are often used to prevent aggregation or agglomeration but may disturb the electronic performance of the final printed product. Thus, the key for ink preparation is to satisfy both dispersion stability and electrical performance.

On the other hand, even if an extended shelf life and manufacturing stability of the suspensions is satisfied, instability may occur in the strong flow in the printing head and may lead to misfiring or even nozzle clogging. In other words, nonjetting can take place even if Z is in the appropriate jettable range; thus, Z alone is incapable of characterizing drop formation. Reis *et al*. (2005) have suggested the drop jettable range for concentrated alumina wax suspensions as $1 < Z < 10$. However, the flow behavior inside the nozzle has been paid less attention.

The clogging during the flow through narrow channels is an extremely complex phenomenon. Such clogging can be caused by a small fraction of aggregates or impurities present in the ink, which are larger than the nozzle diameter (size exclusion). It can be also due to shear-induced gelation in liquid-like colloidal systems [Xie *et al*. (2010), Zaccone *et al*.

(2009, 2010)] or hydrodynamic bridging [Ramachandran and Fogler (1999)], which may occur when several particles arrive at the nozzle entrance simultaneously and make particle bridges, even if these particles are an order of magnitude smaller than the nozzle diameter. This effect is more pronounced when the flow rate is higher. Furthermore, clogging can also occur due to fouling [Wyss *et al*. (2006)], that is, particle deposition at the nozzle wall, and then, it is influenced by the choice of the nozzle material.

1.3 Electrohydrodynamic inkjet printing (EHD)

Electrohydrodynamic (EHD) printing is a complex process in which the charge of the fluid induced by electric field influences the momentum flux of the fluid. By applying high electric potential between capillary tip (or nozzle) and counter electrode, the electrostatic force of the fluid is caused and Taylor cone of conical shape is induced by electric tangential force which is a tangential component of the electrostatic force. Since typical jet diameter formed by this method is smaller than the size of the nozzle by more than one order of magnitude, it enables printing with submicron resolution, mitigating the drawback of piezo-type inkjet printing where droplet size is almost twice of the nozzle size [Li (2006), Kim *et al*. (2007), Park *et al*. (2007), Yudistira *et al*. (2010)] (Fig. 1-3). One practical advantage in EHD printing is that the probability of nozzle clogging is minimalized and charged particles become self-dispersed. It allows the solid content of ink higher than the conventional ink and suppresses the flow-induced aggregation [Lee *et al*. (2012)] which is often caused in piezo-type inkjet printing. Thus, it is applicable in various fields such as bio [Park *et al*. (2008), Ekemen *et al*. (2013)], food [Gomez-Estaca *et al*. (2012), Luo *et al*. (2012)], electronic [Park *et al*. (2007)] and solar cell [Muhammad *et al*. (2011), Park

et al. (2011)], and many more. In contrast to piezo-type inkjet printing where jetting property is determined by the rheological properties of the fluid, in EHD printing where droplet/jet is generated by the electrostatic force, the physical and electrical properties of fluids should also be taken into account in addition to the rheological properties. The electrical and mechanical processing conditions are also crucial variables influencing the quality of jetting/printing.

Ever since the pioneering researches on the drop formation induced by electric field Zeleny (1914, 1917) and Taylor (1964), there have been a lot of analytical and numerical approaches [Barrero *et al*. (1999), Ganan-Calvo *et al*. (1997), Hayati *et al*. (1978a, 1978b)]. Experimental studies have also been done in terms of fluid properties and processing conditions, such as; the size of the droplet relic after jetting with respect to fluid viscosity [Jayasinghe (2002a, 2002b)], the effect of permittivity on droplet size and emitted current [Chen (1997)], the deposition of polymer precursor with respect to flow rates [Grigoriev (2002)], and the deposition of different sizes of particles or functional particles (Fig. 1-4) [Edirisinghe (2004), Yoon *et al*. (2011)].

However, previous studies have mostly been focused on printing performance or simple comparison rather than on the optimization of the

printing system in terms of the fluid properties or processing conditions. Few has attempted to systematically study the Taylor cone of cone-jet mode, which is regarded as an ideal jetting mode for its stable jetting/patterning in EHD printing. In addition, even though the electric tangential force is a decisive factor in forming the Taylor cone and was simulated by Hayati *et al*. (1986, 1987a, 1987b), direct comparison with the experimental results for the cone-jet stability has not been performed.

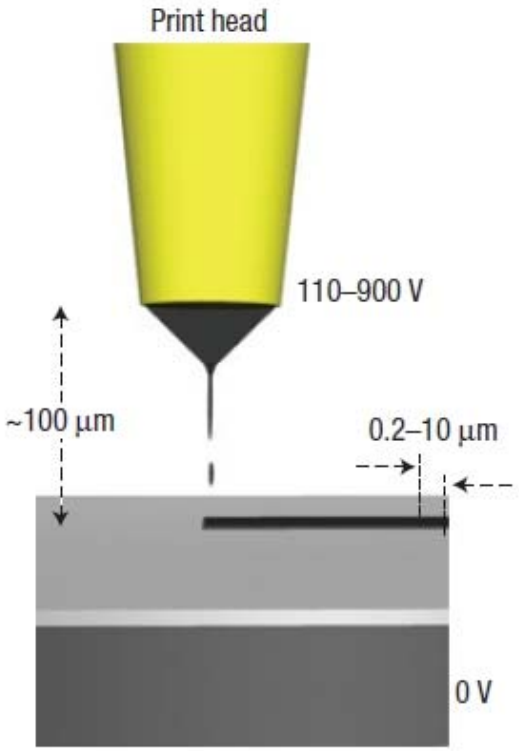

Fig. 1-3 Jetting behavior in electrohydrodynamic (EHD) inkjet printing [Park *et al*. (2007)].

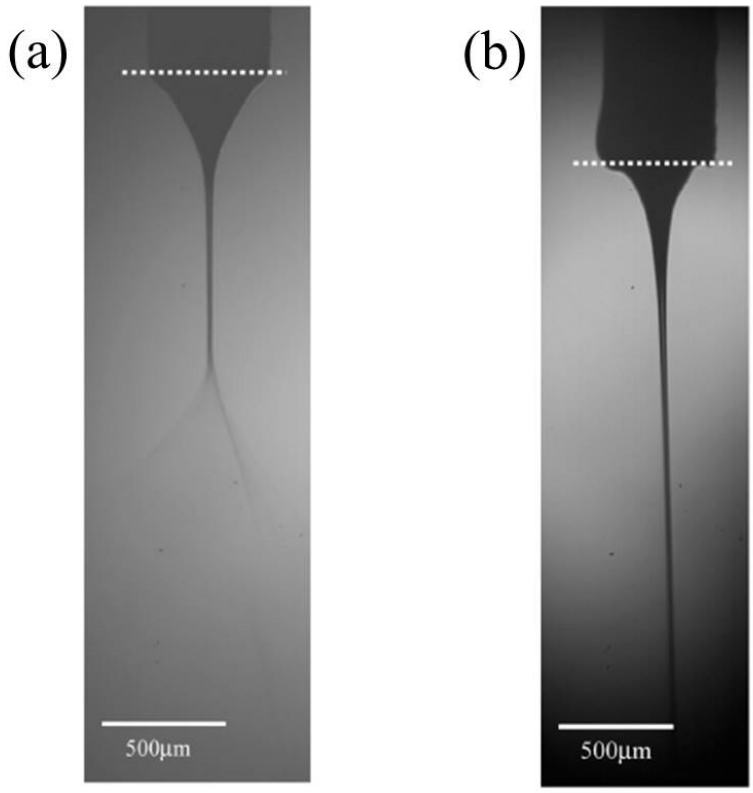

Fig. 1-4 Pictures showing atomization and jet obtained from a) the nano-suspension and b) the micro-suspension. The dotted line indicates the needle exit. [Edirisinghe *et al.* (2004)].

In this study, jetting maps are drawn as a processing window, in terms of the rheological and electrical properties of the fluid, processing conditions, and geometrical configuration. In addition, with the help of numerical simulation, the electrical normal stress $\tau_{E,n}$ and tangential stress $\tau_{E,t}$ acting on the charged surface of Taylor cone are calculated to evaluate the degree of cone-jet stability, and the results are compared with experimental data. The approach is systematic and effective to get Taylor cone of cone-jet mode as a target jetting mode. The control of inks with optimized experimental parameters will improve the jetting performance in EHD printing.

1.4 Objective and outline of the thesis

The harmony of ink (material) and printing method (processing) is of particular importance in producing on-demand droplet and/or inkjet. Thus, the objective of this study is to optimize the printing conditions by understanding the processing characteristics and issues. In piezo inkjet printing (PIJ), nozzle clogging is caused by the use of the functional particulate inks. Therefore, to optimize the experimental parameters for the suppression of the nozzle clogging, the reason for the nonjetting even when the fluid's physical properties are in the appropriate jetting range will be investigated and an additional parameter for the control of the drop jetting of particulate suspension system will be suggested. In electrohydrodynamic inkjet printing (EHD), the electrical properties of the fluids should be taken into account in addition to the rheological properties in order to generate stable cone-jet mode which is the ideal jetting mode. Thus, the development of a systematic method for the formation of the Taylor cone of cone-jet mode and the acquirement of new tools to evaluate the jetting stability will be addressed.

The study is organized as follows.

In chapter 2, theoretical background will be presented in terms of

flow-induced aggregation in PIJ (chapter 2.1) and design of dimensionless groups in EHD (chapter 2.2), respectively. In the drop-on-demand PIJ, based on the relationship between flow-induced aggregation and clogging phenomena from ring-slit device and inkjet printer, the stability of particulate suspensions in converging flow field is investigated. In EHD, six dimensionless parameters are organized as a systematic approach to find the process windows and to apply to the printing system.

In chapter 3, the model fluids, the characterization methods, and the experimental apparatus will be described for PIJ (chapter 3.1) and for EHD (chapter 3.2), respectively.

In chapter 4, ink jettability in PIJ will be analyzed in terms of two issues: ink jettability (chapter 4.1) and stability in converging flow fields (chapter 4.2). In the former, jetting behavior is explored according to various Z ranges, and in the latter, the relationship between flow-induced aggregation and clogging phenomena is discussed in terms of results both from ring-slit device and inkjet printer experiments.

In chapter 5, jet stability in EHD will be presented in terms of three concepts: jetting system (chapter 5.1), jetting map (chapter 5.2), and jet stability (chapter 5.3). In the jet stability, the cone-jet stability is analyzed in terms of dimensionless parameters by comparing the experimental results

with numerical simulation.

In chapter 6, the ideas are addressed regarding ink formulation and nozzle design that help to suppress nozzle clogging in PIJ, and evaluating tools are summarized to obtain the stable Taylor cone of cone-jet mode in EHD to contribute to better design with improved jetting performance in inkjet printing industry.

Chapter 2. Theory

2.1 Flow-induced aggregation in converging flow in PIJ

Recently, it has been shown that heterocoagulation of nanoparticles with micrometer-sized particles can also lead to flow-induced aggregation and clogging in the microchannels. This phenomenon may occur even if the fraction of large particles is on the order of 10−100 ppm and even if these impurities are significantly smaller than the channel dimensions. The larger particles act as nuclei for the aggregation and they are surrounded mostly by small nanoparticles, forming large agglomerates clogging the microchannels [Georgieva *et al*. (2010)]. This phenomenon has been observed even for commercial suspensions with extended shelf life, and it has been identified to cause trouble in filtration, dispensing, or coating operations. A novel equipment called ring slit device has been introduced recently to examine flow-induced aggregation and to characterize the stability of concentrated suspensions exposed to strong flow fields. It has been used not only for

industrial quality control and product development purposes, but also for systematic investigations on the heterocoagulation phenomenon mentioned [Georgieva *et al*. (2010), Ettl *et al*. (2000)].

The ring-slit device embodies a capillary rheometer and ring-slit die. This setup allows a small gap height (10−30 μm), corresponding to a high contraction ratio (≈1:1000) and a large cross-sectional area at the same time. When aggregation takes place, the slit entrance is gradually clogged and this results in a strong pressure increase. Flow conditions can be varied in a wide range and thus can be adapted to match the specific flow process. Variation of the volumetric flow rate, slit height, and entrance angle allows to control the collision frequency and contact time of colliding particles, as well as the total deformation of a fluid element and the velocity gradient in the converging flow region where the aggregation takes place.

Here, we discuss the inkjet printing behavior of colloidal suspensions of inorganic, semiconductive particles. Aqueous formulations of commercial zinc oxide (ZnO) nanoparticles stabilized by a polyelectrolyte-type dispersing agent were used as a model system and printing experiments were performed on a commercial inkjet printer. Suspension stability and inverse Ohnesorge number Z (=Oh^{-1}) were systematically varied over a wide range. These investigations clearly reveal that flow-induced

heterocoagulation due to a small fraction (≈100 ppm) of larger aggregates can cause severe problems during inkjet printing, even if Z is in an appropriate range for jetting of Newtonian fluids.

2.2 Design of dimensionless groups in EHD

2.2.1 Variables

In electrohydrodynamic capillary tip (or nozzle exit), once the fluid meniscus is under electric field, the meniscus deforms, and then the droplet is formed at the capillary tip. This droplet is distorted as electric potential increases by the surface charge, and the conical meniscus is maintained over a certain critical limit of electric potential. At this critical limit of electric potential, the fluid meniscus is balanced by three forces; hydrostatic force F_h which tends to supply more fluid to emerging droplet, capillary force F_γ which tends to hang the droplets at the capillary tip, and electrostatic force F_E which is caused by the electric field (see Fig. 2-1) [Joffre and Cloupeau (1986), Li (2006)].

During this process, the surface charge of the fluid experiences two ways of charge transport - charge conduction and convection - and constant surface charge is maintained by their balance [Hartman *et al*. (1999)].

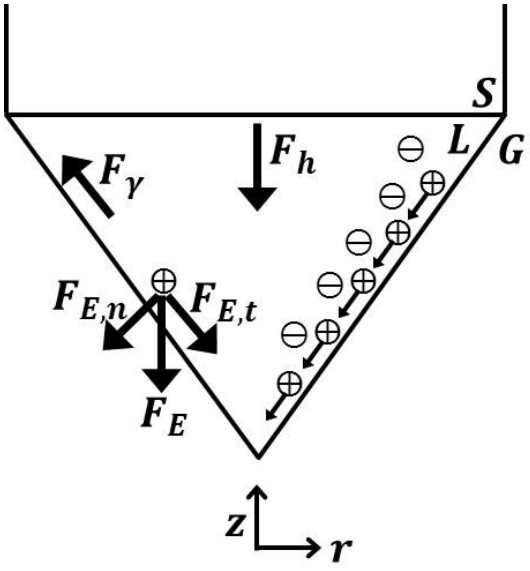

Fig. 2-1 Forces acting on the fluid surface.

Here, the charges move towards the surface, and causes electric normal stress $\tau_{E,n}$. The electric normal force $F_{E,n}$ which works normal outward opposite to the surface tension F_γ which works inward to keep the shape of the droplet. Supplied flow rate Q_s and the electrical charging time which is related to resistance $\sim K^{-1}$ and capacitance $\sim \varepsilon_0 \varepsilon'$ of the system are the variables influencing the charge conduction (where ε_0 is the permittivity of free space, ε' is the fluid permittivity and K is the fluid conductivity) [Park *et al*. (2007)].

The surface charges induced by charge conduction lead to electric tangential stress $\tau_{E,t}$ along the surface meniscus with acceleration toward cone apex. The charge acceleration speeds up the surrounding fluid sequentially, referred to as the charge convection. At this moment, the fluid experiences viscous stress, and as a result, jet is formed by these charge and fluid motions. Then, the variables influencing the charge convection are electric field ($\boldsymbol{E} = V_a/L$, where V_a is the applied voltage and L is the distance between nozzle and counter electrode), permittivity ε' as a charge amount, and viscosity η as a flow resistance.

Here, ten variables are listed below that determine the electrodynamics and fluid dynamics in EHD printing,

$$\rho, \gamma, \varepsilon_0, \varepsilon', K, \eta, d, L, Q_s, V_a \quad (2\text{-}1)$$

where ρ is the density, γ is the surface tension, ε_0 is the permittivity of free space, ε' is the permittivity of the fluid, K is the conductivity, η is the viscosity, d is the nozzle diameter, L is the distance between nozzle and counter-electrode, Q_s is the supplied flow rate and V_a is the applied voltage.

2.2.2 Dimensional analysis

We designed dimensionless numbers to systemize the variables affecting the printing system. The aforementioned ten variables (m = 10) contain four fundamental dimensions (n = 4) - $[M], [\mathrm{L}], [T]$ and $[V]$. Using the Buckingham pi theorem, the number of dimensionless groups equals the number of variables minus the number of fundamental dimensions; m – n= 6. The six dimensionless numbers ($D_1 \sim D_6$) were derived as following,

$$D_1 \sim D_6 = \left(\frac{\varepsilon_0 \varepsilon' Q_s}{d^2 L K}, \frac{\left(\gamma^2 \rho \frac{\varepsilon_0 \varepsilon'}{K}\right)^{\frac{1}{3}}}{\eta}, \varepsilon', \frac{d}{L}, \frac{\rho K Q_s}{\gamma \varepsilon_0 \varepsilon'}, \frac{\sqrt{\varepsilon_0} V_a}{\sqrt{\gamma d}} \right) \tag{2-2}$$

and the designed dimensionless numbers are summarized in Table 2-1 with additional information.

Table 2-1 Design of dimensionless numbers ($D_1 \sim D_6$) governing the system.

Dimensionless groups	D_1	D_2	D_3	D_4	D_5	D_6
Expression	$\frac{\varepsilon_0 \varepsilon' Q_s}{d^2 L K}$	$\frac{\left(\gamma^2 \rho \frac{\varepsilon_0 \varepsilon'}{K}\right)^{1/3}}{\eta}$	ε'	$\frac{d}{L}$	$\frac{\rho K Q_s}{\gamma \varepsilon_0 \varepsilon'}$	$\frac{\sqrt{\varepsilon_0} V_a}{\sqrt{\gamma d}}$
In present notation	$\frac{T_q}{T_h}$	χ	ε'	$\frac{d}{L}$	α	β
Representation	Jetting system	Material property		Geometry	Processing	

Now let us briefly examine the physical meanings of $D_1 \sim D_6 = (T_q/T_h, \chi, \varepsilon', d/L, \alpha, \beta)$.

$D_1 = T_q/T_h$ is the ratio of two characteristic times which determines the jetting system. T_q is the characteristic time of charge transport determined by the electrical properties of the fluid, and T_h is the characteristic time of the fluid supply [Jaworek and Krupa (1999)]:

$$T_q = \frac{\varepsilon_0 \varepsilon'}{K} \tag{2-3}$$

$$T_h = \frac{Ld^2}{Q_s} \tag{2-4}$$

For EHD printing system, charge layer should be developed in the surface, thus the condition $T_q/T_h < 1$ should be satisfied [Ganan-Calvo (1997)]. This will be explained in results and discussion section in detail. D_2 and D_3 are dimensionless numbers linked with materials properties. $D_2 = \chi$ is the ratio of two characteristic velocities; the characteristic velocity of the fluid (Q_c/d^2) and the propagation velocity of a perturbation by viscous diffusion ($\eta/\rho d$),

$$\chi = \frac{Q_c/d^2}{\eta/\rho d} = \frac{\left(\gamma^2 \rho \frac{\varepsilon_0 \varepsilon'}{K}\right)^{1/3}}{\eta} = \frac{\left(\gamma^2 \rho T_q\right)^{1/3}}{\eta} \tag{2-5}$$

where, Q_c is the critical flow rate required for cone-jet formation, and it is

defined as follows.

$$Q_c = \frac{\gamma \varepsilon_0 \varepsilon'}{\rho K} = \frac{\gamma T_q}{\rho} \tag{2-6}$$

$D_3 = \varepsilon'$ is the permittivity of fluid as the amount of the alignment of dipoles. $D_4 = d/L$ is the ratio of nozzle diameter d and nozzle-counter electrode distance L. D_5 and D_6 are the dimensionless numbers linked with processing conditions. $D_5 = Q_s/Q_c = \alpha$ is the dimensionless flow rate defined as the ratio of supplied flow rate Q_s and critical flow rate Q_c. As suggested in eq. (2-6), Q_c is the value determined by the properties of the fluid. This is not simply the amount due to upstream pressure, but rather specific flow rate that causes electrical stress to strip off (or shear) the surface charge layer of the fluid [Mestel (1994)]. $D_6 = V_a/V_c = \beta$ is the dimensionless voltage, which is the ratio of applied voltage V_a and critical voltage V_c, where V_c is the critical voltage that supports the meniscus on the capillary tube of diameter d as follows:

$$V_c = \sqrt{\frac{\gamma d}{\varepsilon_0}} \tag{2-7}$$

Based on the six dimensionless numbers $D_1 \sim D_6 = (T_q/T_h, \chi, \varepsilon', d/L, \alpha, \beta)$ systemized in Table 2-1, we will explore the processing maps in EHD printing. It is again to be noted that the aim of this study is to develop a

systematical method to get the Taylor cone of cone-jet mode and new tools to evaluate the degree of cone-jet stability, based on which the printing process can be optimized.

Chapter 3. Experimental section

3.1 Piezo inkjet printing (PIJ)

3.1.1 Materials

A commercial ZnO powder (VP ADnano ZnO, Evonik degussa) with an active surface of 20−25 m^2/g and a density of 5.6 × 10^3 kg/m^3 was used in this investigation. The primary particles of ZnO powder were in the range of 20 nm, but they practically never isolated and typically formed aggregates, whose effective size was on the order of 100 nm (according to the manufacturer). Distilled water was used as a suspending medium, and a commercial copolymer (Tego Dispers 752W, Evonik Tego Chemie) was used as a stabilizer (in the following we will refer to it as ‘Tego’ for simplicity). It consists of an anionic carboxylated backbone and nonionic polyglycol side chains [Okamura *et al*. (2010), Sis and Birinci (2009), Hommer (2009)]. Dispersions were prepared by adding ZnO solid particles into distilled water with different amounts of stabilizer, which was specified by its mass ratio

relative to the net weight of ZnO. When the ZnO is immersed in water the surface of the oxide is hydrolyzed and a hydroxide layer is built up [Degen and kosec (2000)]. Due to the amphoteric properties of ZnO, it has positive charge under basic conditions when Tego is added to the system, and hydrogen bonding interactions between hydroxyl groups ($-Zn-(OH)^{2+}$) of ZnO and oxygen atoms ($-O-$) of the polyglycol of Tego lead to the adsorption of the stabilizer on the particle surface. Finally, ZnO nanodispersions are electrosterically stabilized by the anionic part of copolymer backbone (see Fig. 3-1).

	Thermodynamic stability	Description
Overall stability	Electrostatic forces by anionic part of PCE (negatively charged backbone)	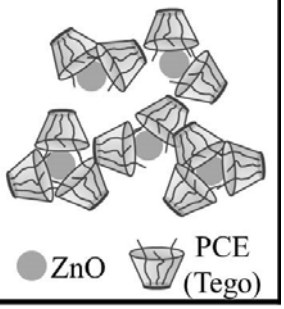
ZnO-Tego	Hydrogen bonding of the hydroxyl groups ($-Zn-(OH)^{2+}$) and oxygen atoms of the polyglycol	

Fig. 3-1 Schematics of electrosterically stabilized ZnO dispersions. Tego is copolymer consisting of polycarboxylate ether (PCE).

The pH dependence of the zeta potential of the neat and the polymer-stabilized ZnO dispersion is shown in Fig. 3-2(a). The neat ZnO shows an isoelectric point (IEP) at a pH of 10.0. The 'ZnO/polymer (Tego)' nanodispersion has an equilibrium pH of 9.0 and a zeta (ζ)-potential of -27 mV and has its IEP at pH of about 7.0.

The average particle size of these ZnO dispersions strongly depends on dispersing conditions. Here, dispersing was aided by ultrasonic treatment using a horn-type ultrasonicator (Digital Sonifier, Brason, U.S.A.). The effect of this ultrasonic treatment is demonstrated for a dispersion of ZnO 2 vol % with Tego/ZnO (w/w) = 0.10 in Fig. 3-2(b). The average particle diameter, as determined by dynamic light scattering, decreases with increasing ultrasonic treatment time (at a constant input power of 32 W) until it finally levels off at about 90 nm after 60 min. Accordingly, all nanodispersions investigated here have been exerted to this ultrasonic treatment procedure. Then they were filtrated with a mesh size of 5 μm (subsequently termed coarse filtration) before printing, unless otherwise stated. Sedimentation can be a problem in long-term storage, but the effect was not significant in our experiments. The inks were used up within one day after preparation, and they were mixed well; they were agitated for a few minutes with a magnetic stirrer and sonicated for 10 min just before

performing the experiments.

To see the influence of the micrometer-sized fraction of aggregates on printing performances, some of the samples for inkjet printing experiments were additionally filtered with 0.45 and 1 μm syringe filters (Acrodisc) (subsequently termed fine filtration) Analogously, samples prepared for the ring slit tests described below were filtered with synthetic woven nanofilament fabric type filters (Sefar NITEX) having mesh sizes of 6 μm (coarse filtration) and 1 μm (fine filtration), respectively. These latter filters were chosen for convenience since ring slit tests require a larger amount of sample (150 mL) compared to inkjet printing experiments (usable ink capacity: up to 1.5 mL).

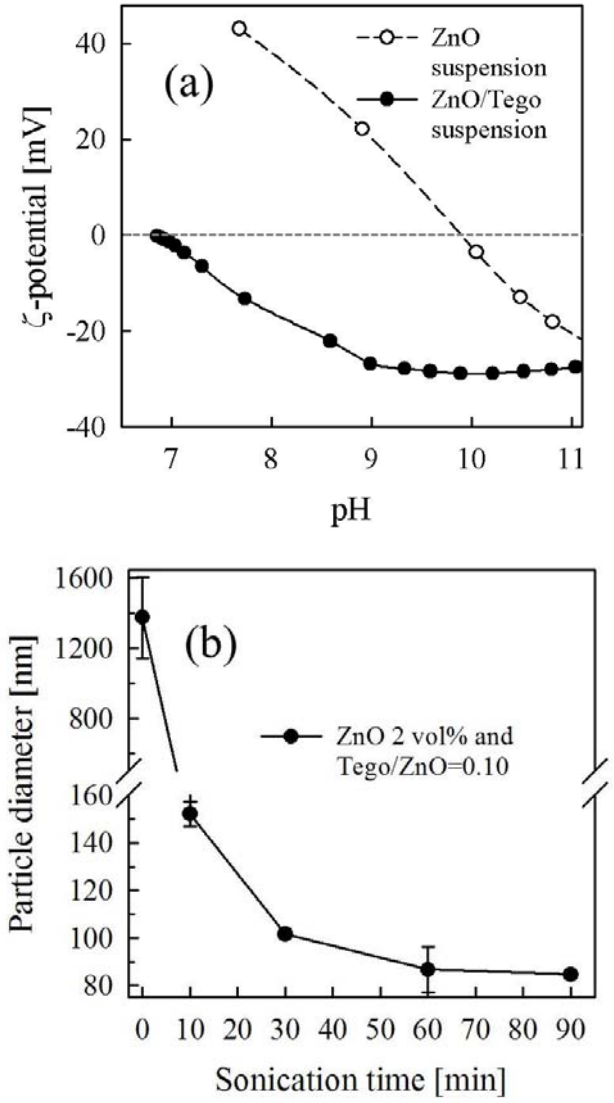

Fig. 3-2 (a) ζ-potential as a function of pH for neat and polymer stabilized ZnO dispersions. (b) Mean particle size by dynamic light scattering for suspensions with 2 vol % ZnO and Tego/ZnO (w/w) = 0.10, and horn-type ultrasonication was conducted as a function of time (at a power of 32 W). The suspension was diluted to 1/300 of the initial concentration to meet the detectable range of the apparatus.

3.1.2 Characterization

Rheological measurements were carried out with a strain-controlled ARES rheometer (TA Instruments, U.S.A.) at shear rate $\dot{\gamma}$ ranging from 1 to 10^3 s^{-1} with cone−plate fixture (gap angle = 0.04 rad, diameter = 50 mm). Surface tension was measured by DCAT tensionmeter (DataPhysics Instruments GmbH, Germany). ζ-potential was measured with an AcoustoSizer IIs (Colloidal Dynamics Pry Ltd., Australia) as a function of pH with titration by using 1 M of HCl and 1 M of NaOH.

Two kinds of devices were used for particle sizing; the Zetasizer Nano ZS (Malvern Instruments Ltd., U.K.), which operates on the principle of dynamic light scattering (DLS), was used to determine the average particle diameter (measurement range 0.3−10 μm); the AccuSizer 780A (PSS, Inc., Santa Barbara, U.S.A.) equipped with a model LE400-05ES particle sensor, which is based on a single particle optical sensing technique (SPOS) counting individual objects in the range 0.5−400 μm, was used to determine the size distribution and total amount of particles/aggregates larger than 0.5 or 1 μm. Data collection was provided by the CW788-Nicomp software (PSS, Inc., Santa Barbara, CA), which accumulates the data in 512 logarithmically spaced channels from minimum to maximum size. The

particle size assigned to a certain channel corresponds to the amplitude of the measured electrical pulse, and together with the number of particle counts for each channel, the total volume of particles in a selected range can be calculated. This technique is especially suitable for detecting and characterizing small fractions of objects larger than the primary particles [Remsen *et al*. (2006)]. All measurements were carried out at room temperature.

3.1.3 Apparatus

3.1.3.1 Inkjet printer

To observe the jetting behavior of ZnO dispersions, the commercial inkjet printer (DMP-2800, FUJIFILM Dimatix Inc., U.S.A.) was used with a 10 pL cartridge, which consists of 16 nozzles (DMC-11610). The smallest area the fluid passes in a cartridge is a circular cross-section with 21.5 μm diameter (according to the manufacturer); a schematic drawing is shown in Fig. 3-3(a). Drops were generated by shear mode actuators based on the reverse piezoelectric effect and observed by a stroboscopic method using LED light for synchronization. We could capture the images of moving drops from the nozzle by changing the delay time between the pulse inception and the flash of LED light. In most cases inkjetting experiments were conducted at a driving voltage of 25 V (maximum applicable voltage is 40 V according to device specification, but for driving electronics a driving voltage of less than 40 V is preferred.).

3.1.3.2 Ring-Slit device

A ring-slit device was used to characterize flow-induced aggregation. We used the setup that has been described in detail earlier [Georgieva *et al*. (2010), Ettl *et al*. (2000)]; a schematic drawing is shown in Fig. 3-3(b). The ring-slit device includes a capillary rheometer (Rosand RH2000, Malvern U.K.) and a homemade stainless steel ring-slit die. The ring-slit height H is fixed as (23 $\pm$ 1) μm in order to match with nozzle size (21.5 μm) of the inkjet printer. This corresponds to a contraction ratio of 1:1000 between the diameter of the sample chamber and the slit height. The sample is forced to flow through the ring-shaped slit with a constant volumetric flow rate Q, which is controlled by setting the piston speed v. A pressure transducer mounted above the die records the corresponding extrusion pressure p as a function of time or extruded sample volume.

If the suspension is stable, the pressure adjusts itself to a comparably low constant value determined by the viscosity of the particular sample. In this case, the instrument operates as a high shear capillary rheometer and the apparent shear rate $\dot{\gamma}_{\mathrm{app}}$, apparent shear stress τ_{app}, and viscosity η_{app} can be calculated as follows [Remsen *et al*. (2006)]:

$$\dot{\gamma}_{\mathrm{app}} = \frac{6Q}{BH^2} \text{ with } Q = \pi R^2 v \tag{3-1}$$

$$\tau_{\text{app}} = \frac{p}{2L/H} \tag{3-2}$$

$$\eta_{\text{app}} = \frac{\tau_{\text{app}}}{\dot{\gamma}_{\text{app}}} \tag{3-3}$$

where R = 12 mm is the radius of the sample chamber, $B = 2\pi R$, and L = 1 mm is the length of the ring-slit. If the suspension is not stable, aggregates gradually clog the slit and the extrusion pressure increases with time. The recorded pressure signal is normalized by the so-called viscous pressure p_{viscous}, which is set equal to the initial pressure reading corresponding to the viscosity of the suspension, so that we only compare the pressure increase caused by the flow-induced aggregation.

Experiments have been done at two different flow rates, 63 mm^3/s and 1574 mm^3/s, as well as two different entrance angles, 45° and 90°, in order to see the effect of flow kinematics and hydrodynamic force on slit clogging. All experiments were conducted at room temperature.

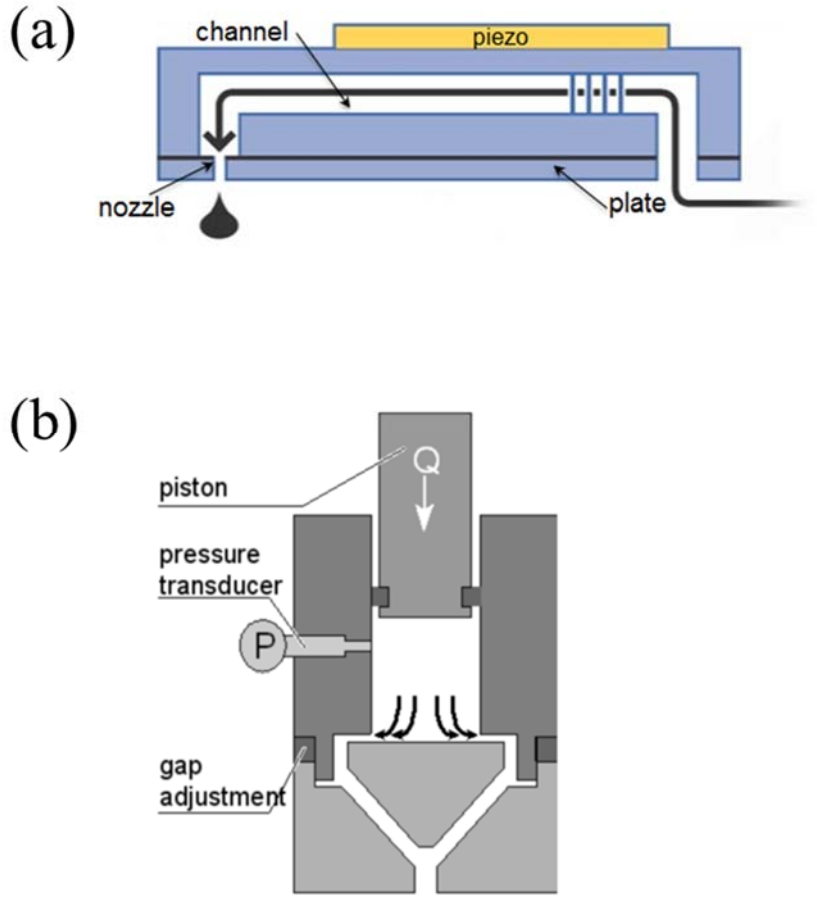

Fig. 3-3 Schematic diagrams of (a) inkjet printer and (b) ring-slit device. Both apparatuses include a contraction channel.

3.2 Electrohydrodynamic inkjet printing (EHD)

3.2.1 Materials

Ethanol (= ethyl alcohol, boiling point: 78^{o}C, dipole moment: 1.6D) and terpineol (= terpene alcohol: 219^{o}C, dipole moment: 1.6~2.0D) were used as model fluids (purchased from Sigma Aldrich). By mixing a different ratio of ethanol (E) and terpineol (T), we could design Newtonian fluids with a wide range of properties. In this paper, we prepared six fluids – E10T0, E8T2, E4T6, E2T8, E0.5T9.5 and E0T10 as a mixture of two fluids. Here, for example, E4T6 means a mixture with ethanol 40 % and terpineol 60 % in volume.

3.2.2 Characterization

Viscosity was measured with a stain-controlled rheometer (ARES, TA Instruments, U.S.A). Surface tension was measured by surface tensionmat (Fisher Scientific, U.K.). Permittivity and conductivity were measured with dielectric analyzer (SI 1260 impedance/gain-phase analyzer and dielectric interface, Solartron, U.K.). All measurements were carried out at room temperature. The measured values of viscosity η, surface tension γ, density ρ, permittivity ε' and conductivity K, and the calculated charge relaxation time T_q, dimensionless velocity χ, critical flow rate Q_c and critical voltage V_c of each fluid are presented in Table 3-1.

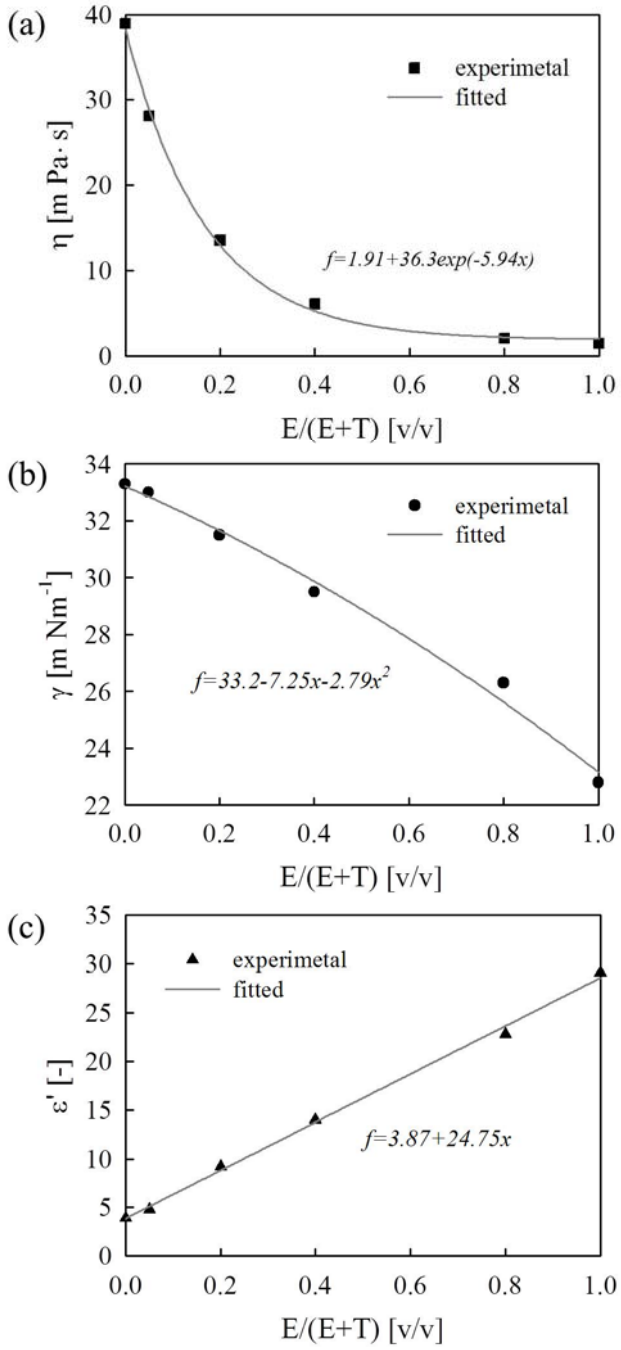

Fig. 3-4 Viscosity, surface tension and permittivity of ethanol/terpineol mixtures.

Table 3-1. Material properties and the characteristic numbers of ethanol/terpineol mixtures.

	E10T0	E8T2	E4T6	E2T8	E0.5T9.5	E0T10
η $[m\ Pa \cdot s]$	1.47	2.08	6.11	13.5	28.1	38.9
γ $[m\ N\ m^{-1}]$	22.8	26.3	29.5	31.5	33	33.3
ρ $[Kg\ m^{-3}]$	789	819	879	909	932	940
ε' $[-]$	29.1	22.8	14.0	9.2	4.8	3.9
K $[S\ m^{-1}]$	1.5×10^{-4}	1.1×10^{-4}	2.3×10^{-5}	1.5×10^{-6}	2.3×10^{-7}	5.0×10^{-11}
T_q $[s]$	1.72×10^{-6}	1.84×10^{-6}	5.39×10^{-6}	5.43×10^{-5}	1.86×10^{-4}	6.94×10^{-1}
χ $[-]$	6.05	4.87	2.62	2.71	2.04	23.0
Q_c $[m^3\ s^{-1}]$	4.96×10^{-11}	5.89×10^{-11}	1.80×10^{-10}	1.88×10^{-9}	6.56×10^{-9}	6.94×10^{-1}
V_c $[kV]$	0.878	0.943	0.999	1.033	1.057	1.062

3.2.3 Printing apparatus

Fluids were injected to stainless steel capillary tube or nozzle (300 μm OD, 180 μm ID) at a constant volumetric flow rate which was adjusted by digitally controlled syringe pump (Longer Pump®, Model LSP02-1B). High voltage power source was connected to stainless steel nozzle and copper plate ground electrode. To observe the jetting behavior, a high-speed camera (Photron fastcam-ultima 512) with 512 x 512 resolution and micro-zoom lens (6.5 X) were used. The light source (MORITEX, 250W Metal Halide lamp) was located opposite to the camera. A schematic drawing of the printing setup is shown in Fig. 3-5.

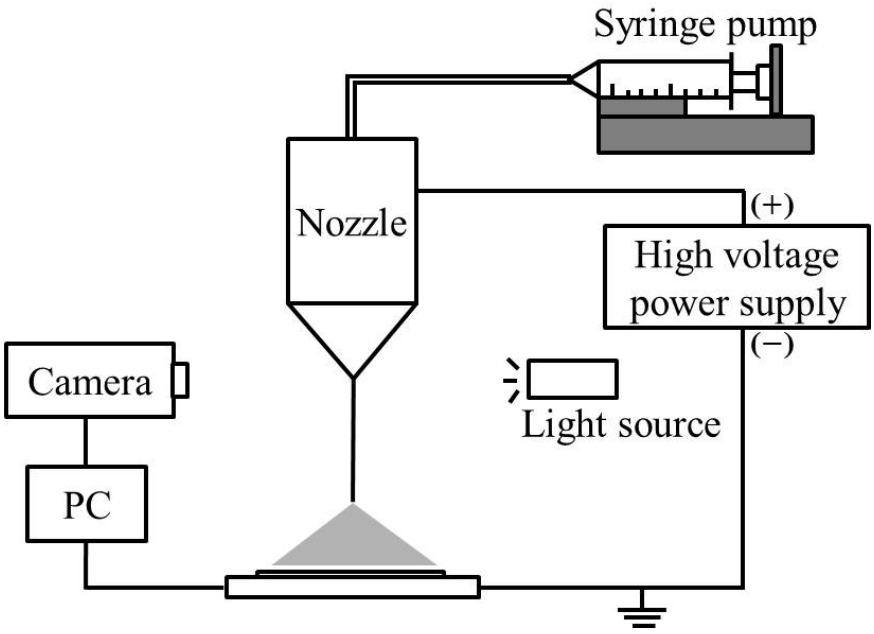

Fig. 3-5 Schematic diagram of EHD printer device. Spray was generated beyond a certain distance after jet formation from the cone apex, which was indicated by gray color.

Chapter 4. Ink jettability in piezo inkjet printing (PIJ)

4.1 Ink jettability

The aim of this study is to tailor printable nanoinks for drop-on-demand inkjet printing. From a fluid mechanics point of view, viscosity η and surface tension σ of the dispersions should be controlled. Viscosity contributes to drop formation by induced pressure wave propagation inside the nozzle, and surface tension contributes to the pinch-off of drops at the nozzle exit. To project droplet at the nozzle orifice, the action of the pressure wave should break the barrier of surface tension.

First of all, to set the various ranges of Z = Oh^{-1} = $Re/We^{1/2}$ = $(d\rho\sigma)^{1/2}/\eta$, the amount of ZnO particles and dispersant Tego were changed. ZnO was added into the distilled water by 2, 10, and 20 vol %, and then, Tego was added by 5−50 wt % in reference to ZnO. For the prepared ZnO suspensions, η, σ, and the dimensionless number Z are summarized in Table 4-1, together with a short comment on printing performance. Viscosity of the

prepared ZnO suspensions is shown in Fig. 4-1. Most of the suspensions showed constant viscosity independent of shear rate, but the suspensions with 20 vol % ZnO exhibited slight shear thinning. In this case, the entries in Table 4-1 correspond to shear rates of 1000 s^{-1}.

According to previous literature [Tai *et al*. (2008), Fakhfouri *et al*. (2009), Tekin *et al*. (2008), Tafreshi *et al*. (2003), Mckinley (2005), Pilch and Erdman (1987), Perelaer *et al*. (2010)], Z is the decisive parameter for judging the jettability in inkjet printing. When Z is too low, drops are not generated due to energy dissipation in the nozzle, while satellite drops are formed during printing when Z is too high. Strictly speaking this criterion can be applied only to Newtonian fluids, while additional concepts should be considered to deal with the jetting performance of particulate suspensions, which include nanoparticles and stabilizers.

The viscosity values obtained can be used to calculate a Péclet number (Pe) for the inkjet printing process to judge the relevance of applied shear forces:

$$\mathrm{Pe} = \frac{\text{Flow force}}{\text{Brownian force}} = \frac{\dot{\gamma}_{wall}}{k_B T/(6\pi\eta a^3)} \tag{4-1}$$

where k_B, T, and η are the Boltzmann constant (1.38×10^{-23} J/K), the temperature (278 K), and the fluid viscosity, respectively. The wall shear rate $\dot{\gamma}_{\mathrm{wall}}$ at the nozzle exit can be calculated from the average drop velocity

$\langle v_x \rangle$, (this quantity depends linearly on the driving voltage, and 25 V corresponds to an average drop velocity of about 5 m/s):

$$\dot{\gamma}_{\text{wall}} = \left| \frac{dv_x}{dr} \right| = \frac{4Q}{\pi R^3}, \text{with } Q = \pi R^2 \langle v_x \rangle \tag{4-2}$$

assuming Newtonian flow behavior. Here, R and a denote nozzle orifice diameter (21.5 μm) and average particle size (85 nm), respectively. Finally, inserting typical values for the suspensions investigated here results in Pe $\approx$ 100−1000, and this implies that the fluids experience strong flow in inkjet printing.

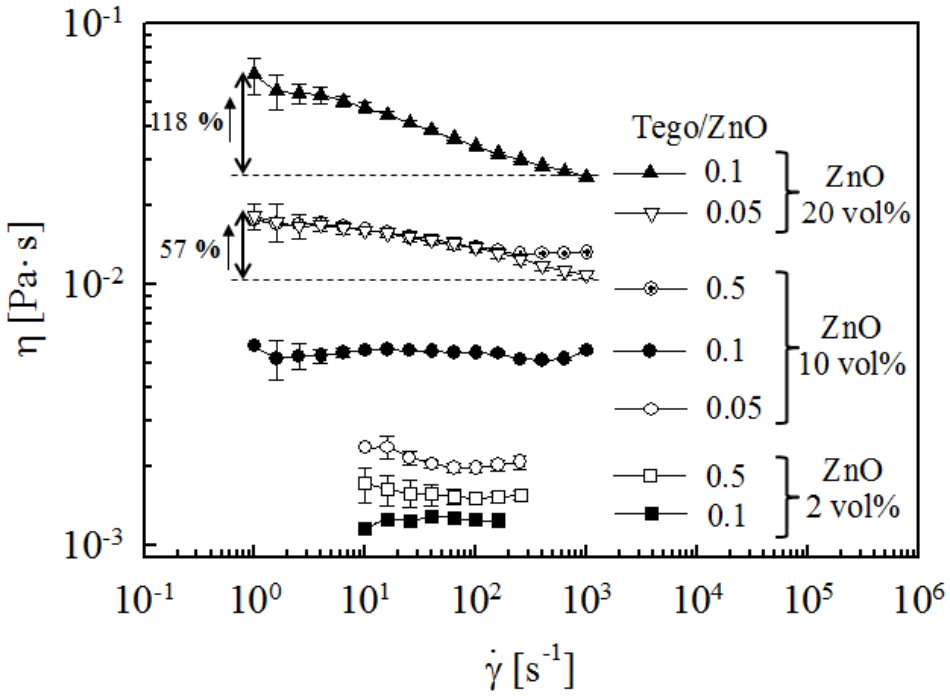

Fig. 4-1 Viscosities of the ZnO suspensions as a function of shear rate.

Table 4-1 Characteristics of the prepared fluids.

Particle	Continuous phase	Stabilizer	Material property			Printing performance
ZnO (vol%)	-	Tego[a]/ZnO (w/w)	η (m Pa-s)	σ (m N/m)	Z (= Oh^{-1})	16 nozzles
2	Water	0.1	1.2	63.1	30	misfiring
		0.5	1.7	55.2	20	jetting (very stable)
	G/W[b,g](20/80)	0.1	2.2	62.5	16	jetting
	DPG/W[c,g](5/95)	0.1	1.3	55.3	26	jetting
10	Water	0.05	2.2	63.6	(†)16	clogging
		0.1	5.4	60.0	6.6	jetting
		0.5	13.2	55.2	2.5	jetting
-	G/W[d](32/68)	-	2.4	68.0	(†)16	jetting
20	Water	0.05	10.7	63.0	(*)3.4	clogging
		0.1	25.8	59.9	(‡)1.4	nonjetting
-	G/W[e](62/38)	-	11.2	65.0	(*)3.4	Jetting
-	G/W[f](76/24)	-	29.0	61.9	(‡)1.4	nonjetting

[a]Tego Dispers 752W, a copolymer consisting of polycarboxylate ether in water at concentration of 50 wt%, free of amino groups, hydroxyl groups, and nonyl phenol ethoxylates [Okamura *et al*. (2010)].

[b]G/W(20/80): The continuous phase was changed as glycerol(G)−water(W) mixture (20%/80%) for adjusting *Z*.

[c]DPG/W(5/95): The continuous phase was changed as dipropyleneglycol(DPG)−water(W) mixture (5%/95%) for adjusting *Z*.

[d]G/W(32/68): Newtonian reference of glycerol(G)−water(W) mixture (32%/68%) for clogging analysis. The value of *Z* is equivalent with that of ZnO 10 vol% with Tego/ZnO = 0.05 ($^{(\dagger)}Z$ = 16).

[e]G/W(62/38): Newtonian reference of glycerol(G)−water(W) mixture (62%/38%) for clogging analysis. The value of *Z* is equivalent with that of ZnO 20 vol% with Tego/ZnO = 0.05 ($^{(*)}Z$ = 3.4).

[f]G/W(76/24): Newtonian reference of glycerol(G)−water(W) mixture (76%/24%) for not-jetting analysis. The value of *Z* is equivalent with that of ZnO 20 vol% with Tego/ZnO = 0.1 ($^{(\ddagger)}Z$ = 1.4).

[g]In material property, viscosity is more changeable by glycerol(G) addition, while surface tension is more susceptible by dipropylene glycol(DPG) addition.

4.1.1 ZnO 2 vol % suspensions

Inkjet printing experiments were conducted for different $Z = (d\rho\sigma)^{1/2}/\eta$ values. Z was varied using different glycerol/water and dipropylenglycol/water mixtures (see Table 4-1).

For 2 vol % ZnO and Tego/ZnO = 0.1 with Z = 30 lots of directional misfiring spray, and very different drop velocities among the 16 nozzles operating simultaneously were observed, as shown in Fig. 4-2(a). However, upon changing Z to Z = 16 and Z = 26 by variation of the solvent, stable drops were ejected.

The system with 2 vol % ZnO and Tego/ZnO = 0.5 (Z = 20) also exhibited stable drop-jetting, as shown in Fig. 4-2(b). Moreover, this system was so well-stabilized that a constant drop velocity was obtained at all nozzles.

These findings reveal that an appropriate intermediate Z range is advantageous for inkjet printing as expected, but even if Z is in the proper range printing, results can be further improved if the colloidal stability of the suspensions is increased (e.g. due to the addition of suitable surfactants).

4.1.2 ZnO 10 vol % suspensions

Inkjet printing experiments were conducted using 10 vol % ZnO suspensions with Tego/ZnO ratios of 0.5 (Z = 2.5) and 0.1 (Z = 6.6). Both suspensions did show good printing results over an extended period of time despite their low Z values.

In contrast, the suspension with the same ZnO concentration but lower Tego/ZnO ratio of 0.05 (Z = 16) exhibited poor jetting for a short period of time, but drops were not ejected anymore after this initial period. In addition, the system did show wetting around the nozzle and accumulation of printed material, as shown in Fig. 4-2(c). In order to confirm that Z = 16 is in the appropriate range for printing, a glycerol/water mixture (32%/68%) with Z = 16 was used as a Newtonian reference, and it was printable perfectly. We suppose that the nonjetting phenomenon is caused by nozzle clogging due to the existence of aggregates or other impurities. Therefore, we conducted fine filtration (with mesh sizes of 0.45 and 1 μm) for the suspension with 10 vol % ZnO and Tego/ZnO = 0.05 (Z =16), and then observed that the drops were ejected without clogging.

Based on these observations, we conclude that even if Z is in the appropriate jettable range drops might not be formed due to nozzle clogging.

Furthermore, we hypothesize that extant micrometer-sized impurities act as nuclei for aggregation in the flow field at the nozzle exit.

This will be discussed in more detail below.

4.1.3 ZnO 20 vol % suspensions

Due to the high particle loading, the viscosity of these suspensions is high, and accordingly, *Z* is low. Moreover, these suspensions exhibit shear thinning. For the suspensions with Tego/ZnO = 0.05 (*Z* = 3.4) and Tego/ZnO = 0.1 (*Z* = 1.4), drops were not ejected at all, as shown in Fig. 4-2(d), even when a maximum voltage of 40 V was applied. To investigate the nonjetting phenomenon observed during printing, glycerol/water mixtures with similar *Z* values (see Table 4-1) were used as Newtonian reference fluids. For the *Z* = 3.4, fluid drops were ejected very well. For *Z* = 1.4, the fluid did not jet at a voltage of 25 V, while it did show drop-jetting at a driving voltage of 40 V for a while, but showed shutoff of the nozzle in the long run, and also did not recover when trying to operate the inkjet printer again.

For the suspension with *Z* = 1.4, three possible mechanisms for nonjetting actuation are suggested here. First, the low value of *Z* corresponds to a high suspension viscosity, which results in a dissipation of the pressure pulse and thus prevents drop-jetting [Reis *et al*. (2005)]. Second, nonjetting might be due to dipole-like flow (doublet flow) caused by a vibrating meniscus. The cause of dipole-like flow is not clear yet, but acoustic streaming by capillary waves or local interfacial tension distortion can be

regarded as the origin (see Fig. 4-3) [Beulen *et al*. (2007), Marmottant and Hilgenfeldt (2003)]. Third, when air bubbles are entrapped in the ink, surface tension increases so that drops are not ejected even when a large amplitude driving voltage is applied [Beulen *et al*. (2007), de Jong *et al*. (2006)].

For the 20 vol % ZnO suspension with Tego/ZnO = 0.05 and $Z = 3.4$, we assume that the observed nozzle clogging is due to flow-induced aggregation resulting from an insufficient colloidal stability, similar to the case of the 10 vol % ZnO suspension with $Z = 16$.

In conclusion, our investigations reveal that for ZnO suspensions drops may be ejected from an inkjet printer if Z is in the range $2.5 < Z < 26$. However, in contrast to Newtonian fluids or weakly viscoelastic polymer solutions, this criterion is not sufficient. For certain suspensions, nonjetting and nozzle clogging were observed presumably due to flow-induced aggregation at the nozzle exit. This may happen if the suspended nanoparticles are not sufficiently stabilized, and aggregation may be promoted by a small fraction of impurities or aggregates much larger than the primary particles, but still smaller than the nozzle diameter of the printer. This hypothesis will be discussed in detail in the next section.

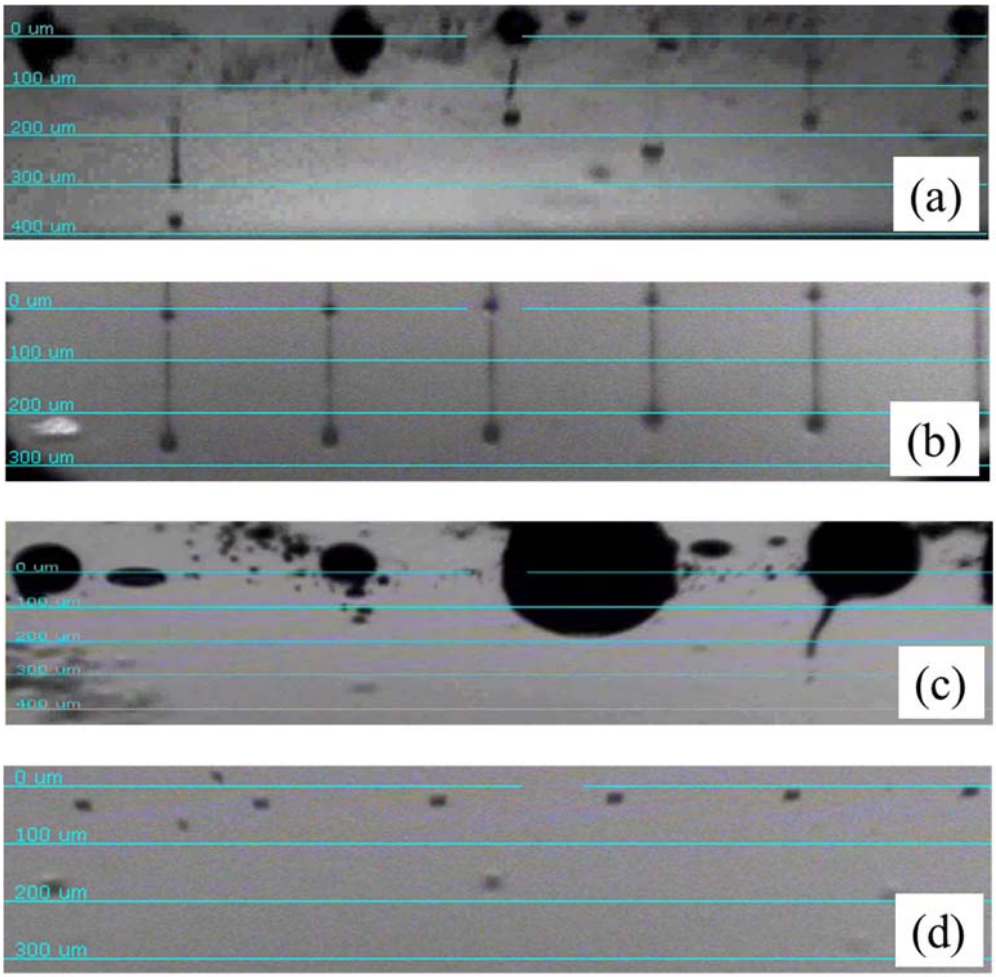

Fig. 4-2 Typical jetting behaviors; (a) misfiring, (b) stable drop-jetting, (c) nozzle clogging, and (d) nonjetting. (a) The suspension with 2 vol % ZnO and Tego/ZnO = 0.1 (Z = 30) showed dissimilar drop velocities and lots of directional misfiring; (b) the suspension of 2 vol % ZnO and Tego/ZnO = 0.5 (Z = 20) resulted in stable drop-jetting in all nozzles; (c) the suspension with 10 vol % ZnO and Tego/ZnO = 0.05 (Z = 16) showed nozzle clogging and never good drop jetting behavior; (d) the suspension with 20 vol % ZnO and Tego/ZnO = 0.1 (Z = 1.4) did not jet from the beginning.

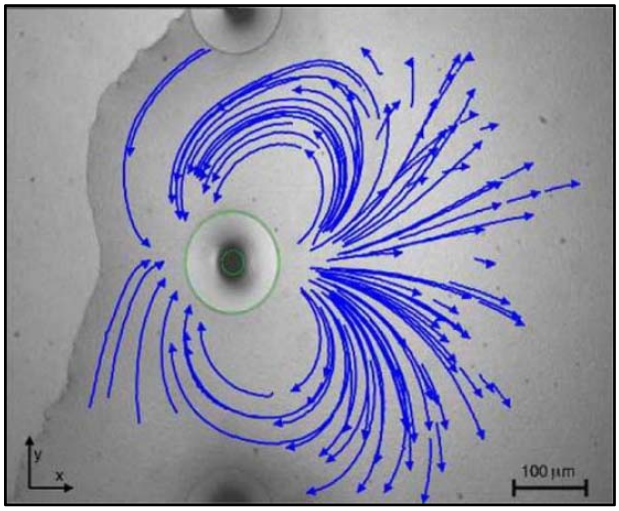

Fig. 4-3 Nonjetting actuation near a nozzle with particle lines of the flow [Beulen (2007)].

4.2 Stability in converging flow fields

4.2.1 Validation of flow similarity between ring-silt device and inkjet printer

We have studied the stability and flow-induced aggregation in contraction flow using a ring-slit device, which was operated under similar conditions as the inkjet printer regarding flow velocity v_x and slit height H or nozzle diameter D. First of all, to validate the flow similarity between these two types of apparatus, namely the inkjet printer and the ring-slit device, the output performance for two suspensions of similar intermediate Z ranges (Z = 16 and Z = 20) was compared. As a result, the suspension that formed stable drop-jetting in inkjet printing did show a constant pressure signal in the ring-slit test, while the suspension that caused nozzle clogging in inkjet printing exhibited a dramatic pressure increase in the ring-slit test. In other words, the flow similarity in these two apparatus was verified reasonably (see Fig. 4-4). At a driving voltage of 25 V, wall shear rates $\dot{\gamma}_{\text{wall}}$ in the nozzle are on the order of 10^5 s^{-1}. The shear rate in the slit channel depends on the applied piston speed; it corresponds to 11 000 s^{-1} at a flow rate of 63 mm^3/s and 280 000 s^{-1} at a flow rate of 1574 mm^3/s (eq. (3-1)).

According to Wang *et al*. (2012), the shear rate in the nozzle is on the order of 10^5 s^{-1} for the first few microseconds but then quickly drops to 10^4 s^{-1} after about 15 μs. Thus, we think the deformation rates in both devices are matched well.

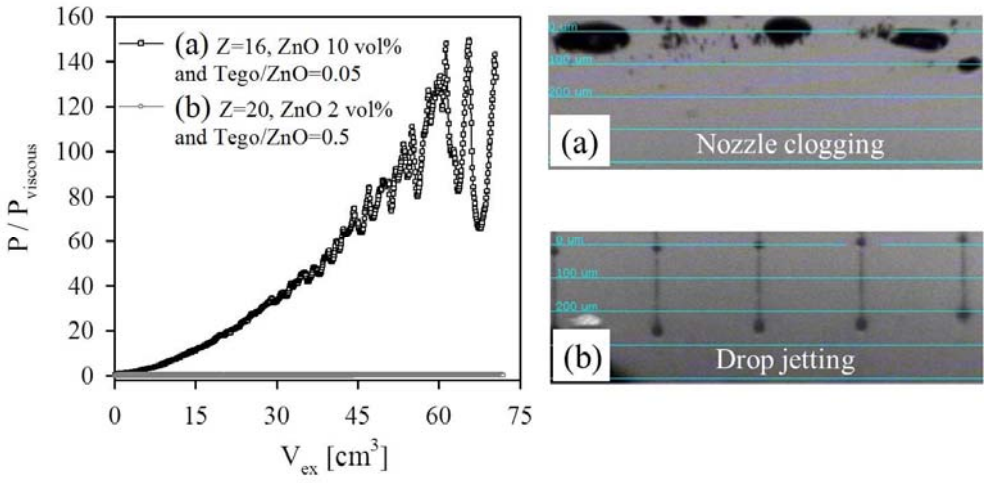

Fig. 4-4 Comparison of flow behavior in ring-slit device (left) and inkjet printer (right) for the suspensions of similar, intermediate *Z* values (*Z* = 16 and *Z* = 20). (a) The suspension that shows nozzle clogging exhibits a dramatic pressure increase, while (b) the suspension that shows stable drop-jetting shows a constant pressure signal.

4.2.2 Flow-induced aggregation in slit and nozzle entrance

In the light of previous investigations on concentrated polymer dispersions [Georgieva *et al*. (2010)], we anticipate that nozzle clogging observed for the ZnO suspensions in inkjet printing is a result of flow-induced aggregation, and this phenomenon is promoted by a small fraction of micrometer-sized impurities.

To demonstrate the effect of such impurities or aggregates on clogging, pressure profiles were examined for suspensions with Z = 16 and Z = 3.4 (which led to nozzle clogging) prefiltered with different mesh sizes (coarse (6 μm) and fine (1 μm) filter), as shown in Fig. 4-5. The coarse filtered suspensions did show strong pressure increase, while the fine filtered suspensions exhibited only a weak, linear pressure increase. From these results, we conclude that aggregates in the size range between 1 and 6 μm are decisive for the observed clogging phenomenon.

This is in line with previous investigations revealing that the number density of particles larger than 0.5 or 1 μm is a crucial factor that may cause trouble during jetting [Shakhnovich and Belmont (2009)].

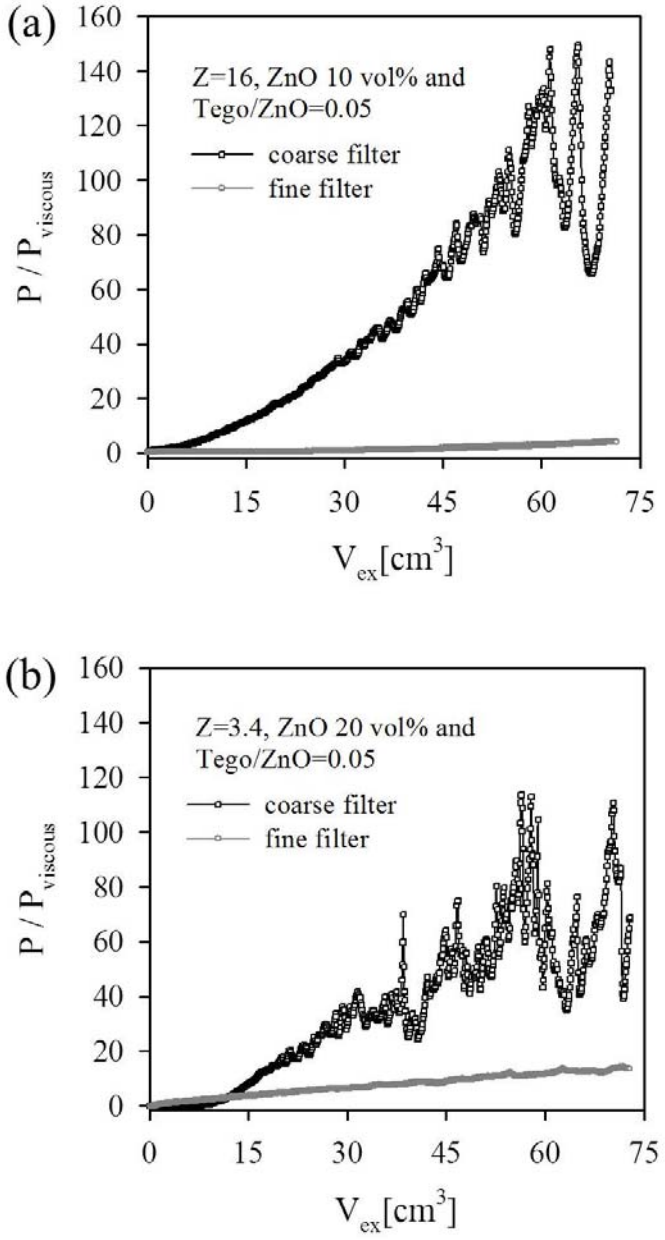

Fig. 4-5 (a) Effect of filtration efficiency on pressure development for suspensions with (a) 10 vol % ZnO and Tego/ZnO = 0.05 (Z = 16) and (b) 20 vol % ZnO and Tego/ZnO = 0.05 (Z = 3.4) at flow rate = 63 mm^3/s.

We have investigated the colloidal stability of ZnO suspensions using a single particle optical sensing (SPOS) technique. This technique is used to characterize the size distribution and total amount of extant impurities/aggregates larger than 0.5 or 1 μm quantitatively, which are supposed to be decisive parameters for nozzle clogging.

Results for the suspensions with 10 vol % ZnO and Tego/ZnO = 0.05 as well as 20 vol % ZnO and Tego/ZnO = 0.05, which exhibited slit clogging are shown in Fig. 4-6. Prefiltration with the fine filter shifted the particle size distribution to lower values compared to the coarse filtration as expected.

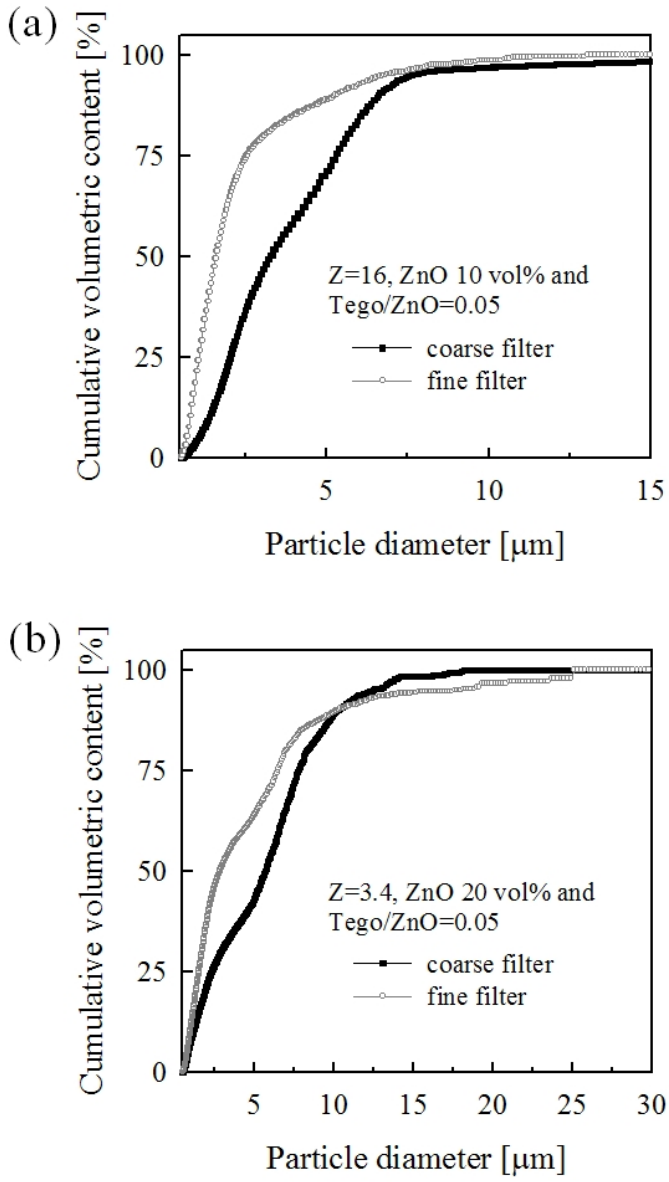

Fig. 4-6 Cumulative volumetric distributions of micron-sized particles for suspensions with (a) 10 vol % ZnO and Tego/ZnO = 0.05 (Z = 16) and (b) 20 vol % ZnO and Tego/ZnO = 0.05 (Z = 3.4) by single particle optical sensing (SPOS) technique.

The measured values for the fraction of aggregates larger than 1 μm $\varphi_{\text{aggregates}} = V_{\text{aggregates}}/V_{\text{dispersion}}$ normalized by the total volume fraction of solids φ_{initial} as well as the total number of particles larger than 1 μm found in different suspensions are summarized in Table 4-2. As expected, the relative volume fraction and the number of aggregates increase with increasing solids content. At fixed ZnO concentration the relative volume fraction and number of aggregates decreases with increasing amount of stabilizer. Finally, the relative volume fraction and number of aggregates decreases with decreasing filter mesh size at fixed ZnO and stabilizer concentration.

Table 4-2 Quantitative analysis of aggregates for ZnO suspensions by SPOS technique.

ZnO in vol %	2		10					20
mTego/mZnO (w/w)	0.1	0.5	0.05			0.1	0.5	0.1
	w/o filter	w/o filter	w/o filter	coarse filter	fine filter	w/o filter	w/o filter	w/o filter
$(\varphi_{aggregates}/\varphi_{initial}) \times 10^{-6}$ (≥ 1 μm)	315	260	620	500	360	560	360	830
no. aggregates (≥ 1 μm) (10^5 aggregates/$mL_{dispersion}$)	2.32	2.01	7.42	7.11	4.86	6.43	6.85	18.3

These results from SPOS analysis are as expected, and they further confirm that the fraction and number of aggregates in the micrometer range is crucial for nozzle clogging during inkjet printing. For the ZnO suspensions investigated here, the relative volume fraction of aggregates $\geq 1\ \mu m$ should not exceed 500 ppm and their total number should be below 7×10^5/mL in order to avoid clogging.

Now the question remains whether nozzle clogging is due to flow-induced homocoagulation between micrometer-sized impurities or heterocoagulation between these impurities. This phenomenon has been investigated carefully for a series of different concentrated polymer dispersions, and it could be clearly shown that heterocoagulation is the mechanism controlling nozzle clogging in these systems [Georgieva *et al*. (2010)]. The most important argument, which also holds for the ZnO suspensions investigated here, is that the collision probability between micrometer-sized impurities is extremely low, since it is proportional to their concentration squared. Therefore, homocoagulation of the large objects is unlikely. We, therefore, propose that heterocoagulation takes place between micrometer-sized impurities and nanoparticles of ZnO in the elongational flow field at the nozzle exit (similar to that observed by Georgieva *et al*. (2010)), even if the size of these impurities is smaller than the size of the

nozzle gap or slit height, and that this is the origin of nozzle clogging finally preventing proper inkjet printing.

To examine the flow-induced aggregation mechanism from a perspective of processing conditions, the effects of flow rate and entrance angle on extrusion through the ring-slit device were investigated for two suspensions that exhibited clogging phenomena in inkjet printing. The corresponding results are shown in Fig. 4-7 and Fig. 4-8. For both suspensions, the pressure increase was much more pronounced at the lower flow rate (63 mm^3/s) and an almost stable pressure signal was observed at the higher flow rate (1574 mm^3/s). These results further support that nozzle clogging is not due to hydrodynamic bridging (clogging would then be more pronounced at higher flow rate) but by flow-induced aggregation. Applying higher flow rates results in a break-up of aggregates and might be compared with a purging process where large air pressure is applied to remove residual impurities inside the nozzle. The entrance angle also had a strong effect on slit clogging, as can be seen from Fig. 4-8. The larger entrance angle (90°) resulted in a better stability than a smaller entrance angle (45°). For this purpose we used the commercial software COMSOL Multiphysics (COMSOL 4.2, Comsol Inc., U.S.A.). The 2D axisymmetric simulations were focused on the contracting region at the entrance of the slit (see Fig. 4-

9). This is in line with the results already reported [Georgieva *et al*. (2010)] and may be attributed to the shorter time of exposure to the elongational flow field, which is especially relevant for well-stabilized systems, where particles need a certain minimum contact time in order to form aggregates.

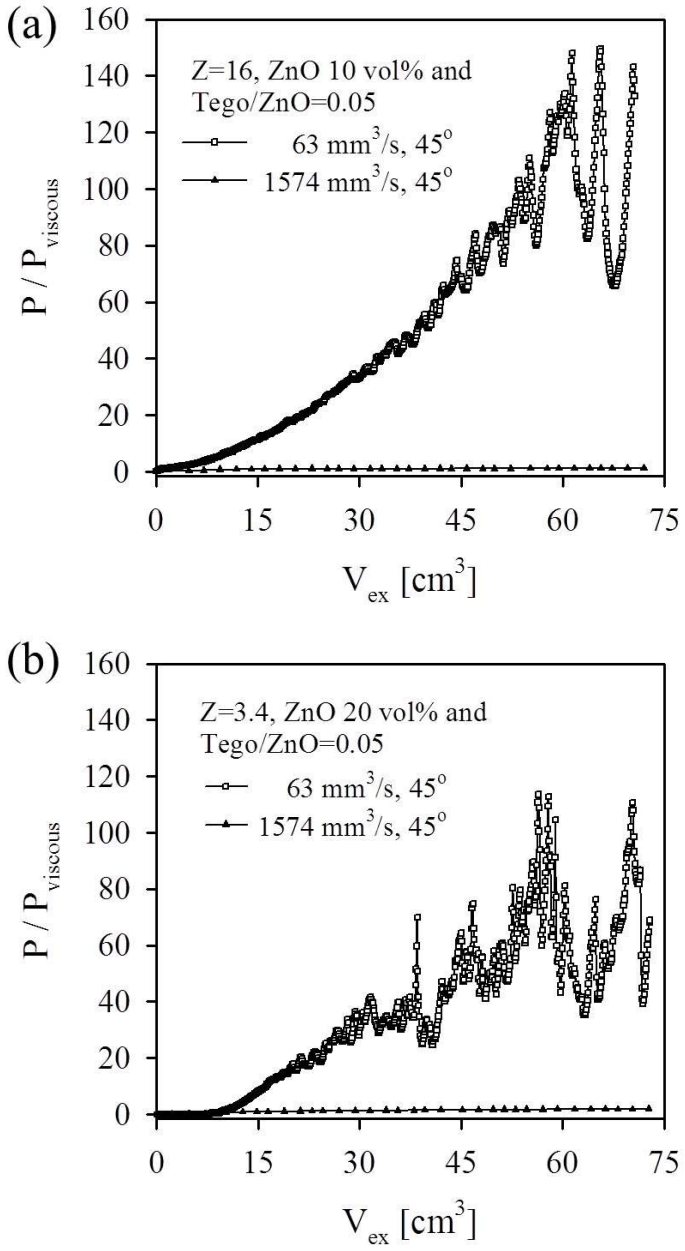

Fig. 4-7 Effect of flow rate on flow-induced aggregation for suspensions with (a) 10 vol % ZnO and Tego/ZnO = 0.05 (Z = 16) and (b) 20 vol % ZnO and Tego/ZnO = 0.05 (Z = 3.4).

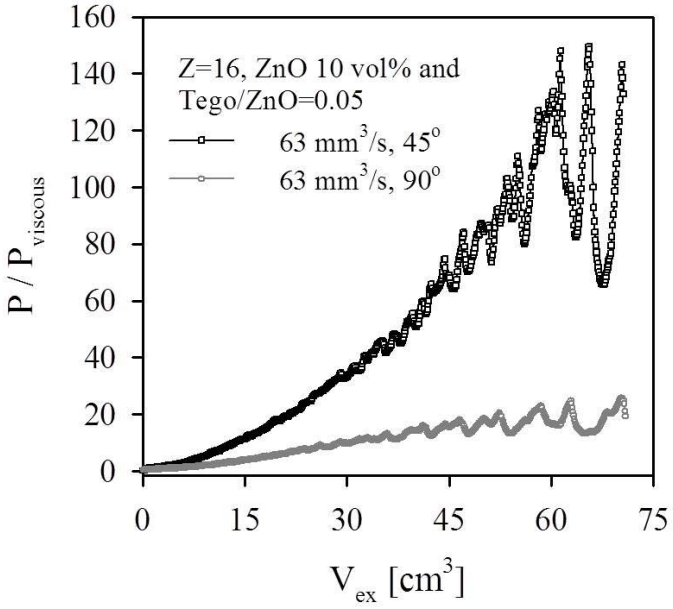

Fig. 4-8 Effect of entrance angle on flow-induced aggregation for suspensions with 10 vol % ZnO and Tego/ZnO = 0.05 (Z = 16).

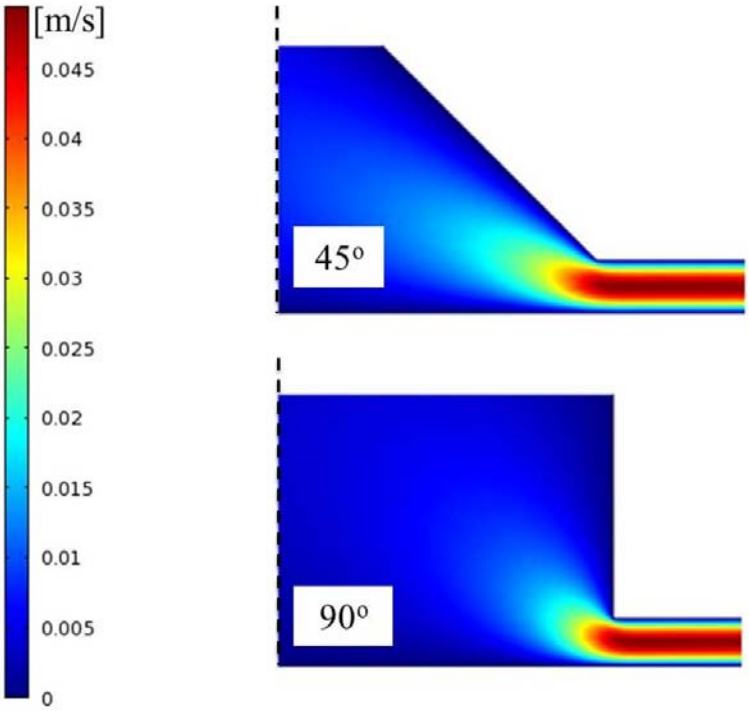

Fig. 4-9 Computed velocity field at entrance angles of 90° and 45° for 10 vol % ZnO and Tego/ZnO = 0.05 (Z = 16).

Chapter 5. Jet stability in electrohydrodynamic inkjet printing (EHD)

5.1 Jetting system

The jetting system is determined by the magnitude of T_q/T_h which is the ratio of two characterization times, charge relaxation time ($T_q = \varepsilon_0\varepsilon'/K$) and hydrodynamic time ($T_h = Ld^2/Q_s$). If $T_q/T_h < 1$, the charge relaxation time is shorter than the fluid supply time by the syringe pump, thus enough free charge (plus induced charge) builds up enough below the liquid-gas interface, thereby forming a thin layer of charges. Thus, stable cone-jet mode can be generated when physical conditions are optimized (see Fig. 5-1(a)). This is categorized as classical electrohydrodynamic (EHD) jetting system [Ganan-Calvo (1997), Muhammad *et al*. (2011)]. When the condition for EHD jetting is satisfied as $T_q/T_h < 1$, electrospinning can also take place for polymer solutions or melts [Deitzel *et al*. (2001), Shin *et al*. (2001), Theron *et al*. (2004)].

On the other hand, if $T_q/T_h > 1$, the supply of the fluid prevails

over the charge transport to the fluid surface, and as a result, the electrostatic force from the charge buildup does not dominate the jetting system. At this time, the electric field plays the role of accelerating the jet which was already generated, rather than contributing to the jet formation. Thus, it is categorized as non-classical EHD system, which is newly defined electrically forced jet. In addition, the ball-cone (cone-like bulging drop) can be observed for the fluids with low conductivity (K~10^{-10} S m^{-1}) [Jayasinghe and Edirisinghe (2004a, 2004b)] (see Fig. 5-1(b)). In this case, since the charges in bulk fluid are not sufficient to induce surface charges, low electrophoretic force is caused, and instead, the dielectrophoretic force by charge polarization moves the fluid to capillarity tip (or nozzle exit) as a region of highest field intensity [Hayati *et al*. (1987)].

In the T_q/T_h, which judges the jetting system, when geometrical configuration is fixed (in this study $d = 300\,\mu$m and $L = 25$ mm), the supplied flow rate $Q_s\,(=\alpha Q_c)$ is the crucial factor for determination of jetting system. Since the critical flow rate $Q_c(=\gamma\varepsilon_0\varepsilon'/\rho K)$ is the designated value by fluid, the dimensionless flow rate α eventually determines the jetting system as presented in eq. (5-1).

$$D_1 = \frac{T_q}{T_h} = \frac{\varepsilon_o\varepsilon'/K}{Ld^2/Q_s(=\alpha Q_c)} = \frac{\gamma}{Ld^2\rho}\left(\frac{\varepsilon_o\varepsilon'}{K}\right)^2 \alpha \qquad (5\text{-}1)$$

The magnitude of T_q/T_h is calculated with respect to α by eq. (5-1), and as a result, the jetting system can be categorized as in Fig. 5-1(c). Here, white region is for classical EHD jetting ($T_q/T_h < 1$) and grey region is for newly defined electrically forced jet system ($T_q/T_h > 1$). As our attention is directed to classical EHD jetting system in this paper, the condition of $T_q/T_h < 1$ should be satisfied.

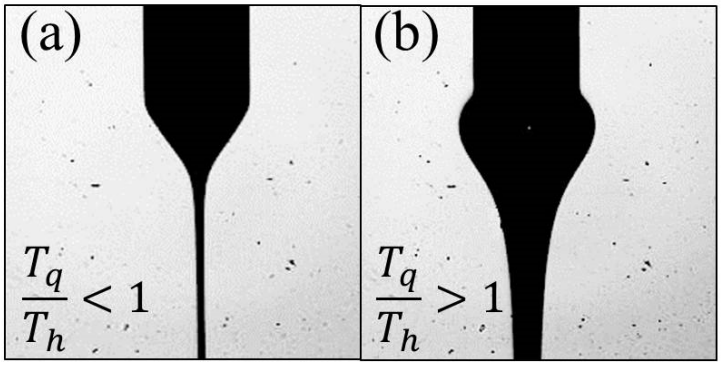

(c)	E10T0	E8T2	E4T6	E2T8	E0.5T9.5	E0T10
$\alpha = 0.1$						
$\alpha = 0.5$		$\frac{T_q}{T_h} < 1$			$\frac{T_q}{T_h} > 1$	
$\alpha = 1$						
$\alpha = 5$						
$\alpha = 10$						

Fig. 5-1 The shape of (a) cone-jet (if $T_q/T_h < 1$) and (b) ball cone (if $T_q/T_h > 1$). (c) jetting window with respect to α for each fluid; white region is for classical EHD system and grey region is for electrically forced jet system.

5.2 Jetting map

The fluid is supplied inside the nozzle by syringe pump, and is simultaneously taken out of the nozzle by applied electric field between the nozzle and the counter electrode. This supply and loss balance of the fluid affects the shape and volume of the cone-jet. Processing parameters are D_5 $(= Q_s/Q_c = \alpha,$ where $Q_c = \gamma\varepsilon_0\varepsilon'/\rho K)$ and D_6 $(= V_s/V_c = \beta,$ where $V_c = \sqrt{\gamma d/\varepsilon_0})$. Q_c is the key parameter for cone-jet formation [Choi *et al*. (2011), Muhammad *et al*. (2011)]. When $\alpha = 1$, the stable jet can be generated from the balance of flux strength and electric field strength. By setting $\alpha = 1$, we found the specific electric potential (i.e. controlled β) at which the stable jet was generated, and explained jetting behavior in terms of α and β as shown in Fig. 5-2.

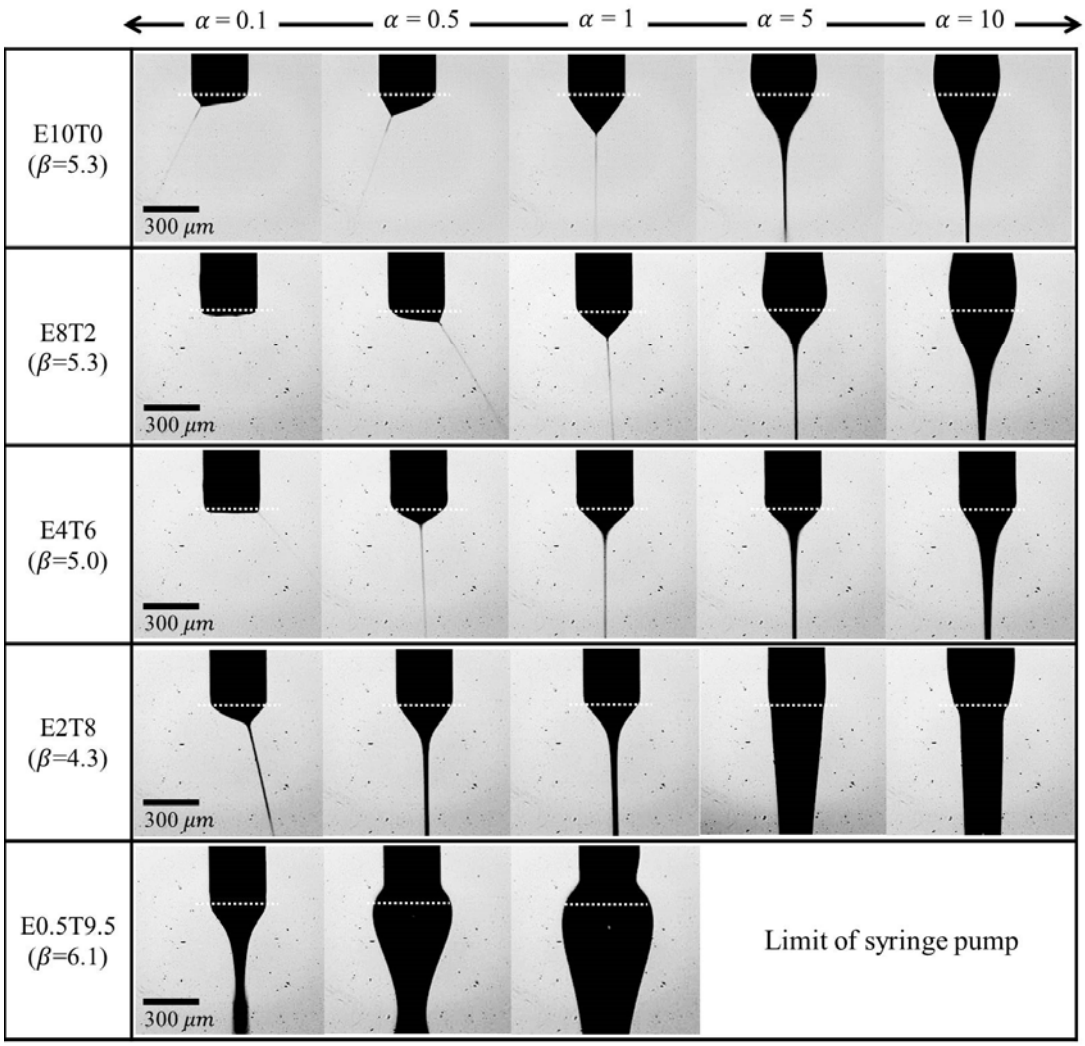

Fig. 5-2 Jetting behavior of the fluids (E10T0 / E8T2 / E4T6 / E2T8 / E0.5T9.5) in terms of processing parameters; dimensionless flow rate α and dimensionless voltage β. To distinguish the position of the nozzle exit, dotted lines were marked in white color.

Since E10T0, E8T2 and E4T6 belong to EHD jetting range ($T_q/T_h < 1$) as shown in Fig. 5-1(c), the Taylor cone of stable cone-jet mode was generated under the condition of controlled β at $\alpha = 1$. On the other hand, under the same condition, the jet was not formed or was not straight but bended for $\alpha < 1$. The Taylor cone was generated but thickening of jet diameter was observed for $\alpha > 1$ (see Fig. 5-2).

In case of E2T8, both systems of EHD jetting ($T_q/T_h < 1$) and electrically forced jet ($T_q/T_h > 1$) are allowed as shown in Fig. 5-1(c). Compared to the other fluids, stable Taylor cone was generated at $\alpha = 1$ and even at much lower flow rate $\alpha = 0.5$. Even though the region of $\alpha > 1$ corresponded to electrically forced jet system, the ball-cone was not observed and jet diameter was almost the same as the nozzle diameter (see Fig. 5-2). It means that the electric field affects the jet acceleration only, and does not contribute to the jet formation at this condition.

For E0.5T9.5, the cone-jet mode appeared (with spray in lower part) at $\alpha = 0.1$ and ball-cone was observed for α larger than 0.5 (see Fig. 5-2). That is, two jetting systems appeared depending on α, and they are well matched with jetting window of Fig. 5-1(c). When α is larger than 0.1, the fluid climbed up the nozzle wall (see the dotted line in the figure). For E0T10, the system corresponds to electrically forced jet because $T_q/T_h > 1$,

thus ball-cone should appear at all α. However we could confirm the ball-cone formation only at small α due to the limit of Q_s.

In Fig. 5-2, in terms of cone-jet shape, when it satisfies the condition of $T_q/T_h > 1$, E10T0 and E8T2 which have relatively high conductivity (K~10^{-4} $S\ m^{-1}$) showed clear jet formation at meniscus apex. On the other hand, for E4T6 and E2T8 which have relatively lower conductivity (10^{-5}~10^{-6} $S\ m^{-1}$), the distinction was not clear between cone and jet [Cloupeau and Prunetfoch (1989)]. When it satisfies the condition $T_q/T_h < 1$, either a jet whose diameter is the same as the nozzle diameter or a ball-cone was formed. The indicated β of Fig. 5-2 is the controlled value for stable Taylor cone of cone-jet mode at $\alpha = 1$. In practice, the electric potential as well as the flow rate affects the jetting behavior significantly, and the jetting behavior depends on the rheological and electrical properties of the fluid too.

In classical EHD jetting system ($T_q/T_h < 1$), a variety of jetting modes can be generated with respect to the electric potential as shown in Fig. 5-3. The increase of electric potential generally leads to a sequence of jetting modes; dripping, pulsating, cone-jet, tilted-jet, twin jet and multi-jet.

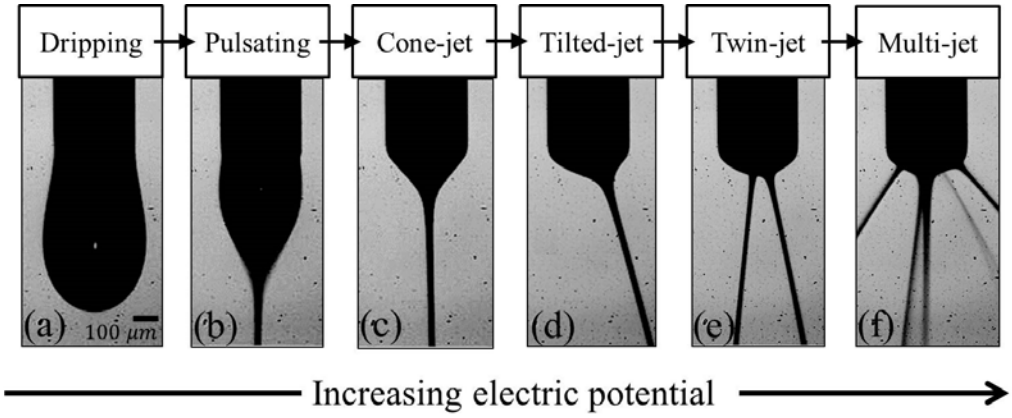

Fig. 5-3 EHD jetting modes with respect to electric potential.

In dripping mode, the pendant drops pinch off from nozzle end due to the gravitational force. Added electrostatic force by electric field counters the surface tension force and helps gravitational force to pinch off the droplets more rapidly. In pulsating mode (or spindle mode), the hemispherical shape and Taylor cone shape are repeated due to the imbalance of the surface tension and the electric charge of the ions. Cone-jet mode is the case when Taylor cone is formed consistently and constant jet emerges from cone apex as an ideal jetting mode in EHD printing. In addition, the increase in electric field results in imbalance between the forces, thus jet leans towards one side, which is called tilted-jet mode. Next, twin-jet mode is brought out forming two jets. Further increase of electric potential causes excessive charges on the cone, and as a result, the accumulated charges reach the limit and multi-jet mode is generated to minimize the energies by rearranging them to large areas [Ashgriz (2011), Yoon *et al*. (2011)]. In this study, multi-jet is defined as Taylor cone shrinkage and the meniscus becomes flat with more than three jets.

For comparison, we suggest jetting modes of electrically forced jet system ($T_q/T_h < 1$) as dripping, ball-cone and multi-jet modes with respect to increasing electric potential in Fig. 5-4.

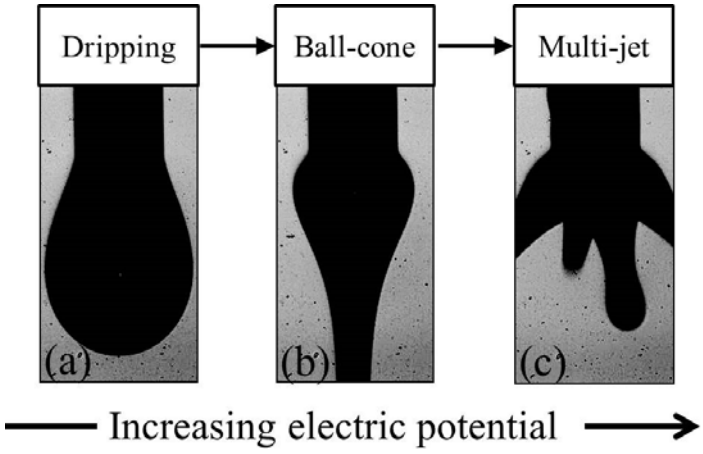

Fig. 5-4 Jetting modes of electrically forced jet with respect to electric potential.

Let us now draw jetting/operating maps based on various jetting modes of classical EHD in terms of six dimensionless parameters $D_1 \sim D_6 = (T_q/T_h, \chi, \varepsilon', d/L, \alpha, \beta)$. Jetting maps for Newtonian fluids of E10T0, E8T2, E4T6 and E2T8 including classified jetting modes (a) ~ (f) (see Fig. 5-3) are drawn in Fig. 5-5.

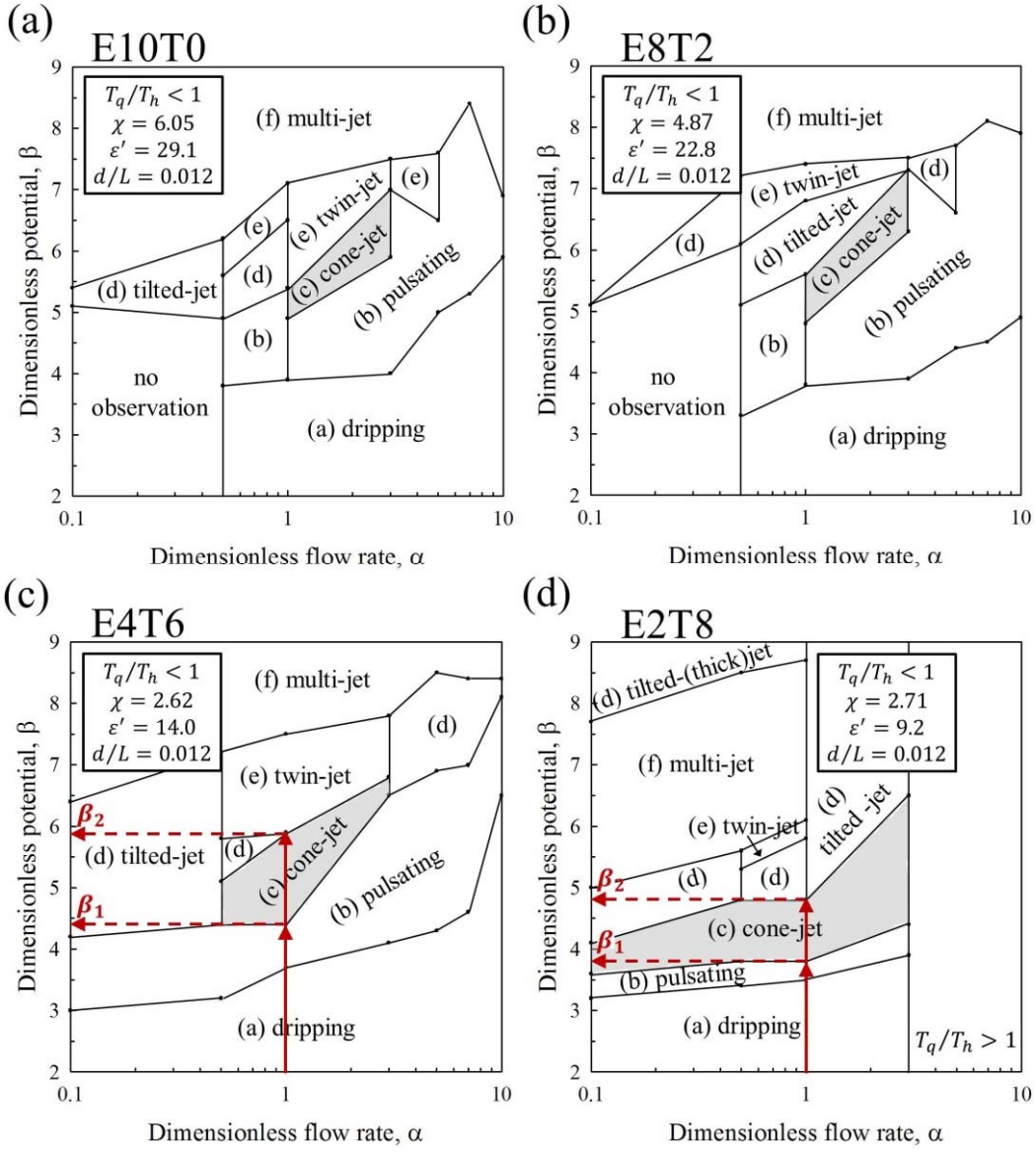

Fig. 5-5 Jetting maps in terms of the dimensionless numbers $D_1 \sim D_6 = (T_q/T_h, \chi, \varepsilon', d/L, \alpha, \beta)$ for (a) E10T0 ($\chi = 6.05$, $\varepsilon' = 29.1$), (b) E8T2 ($\chi = 4.87$, $\varepsilon' = 22.8$), (c) E4T6 ($\chi = 2.62$, $\varepsilon' = 14.0$), and (d) E2T8 ($\chi = 2.71$, $\varepsilon' = 9.2$). Classified jetting modes (a) ~ (f) of Fig. 5-3 are indicated in the map.

It should be noted that not all the jetting modes appear in all the fluid systems due to the difference in processing parameters and fluid properties. For $\alpha < 1$ in E10T0 and E8T2, the jet never appeared at low β and cone-jet mode was not generated. The increase of β ultimately led to multi-jet mode for all the fluids, but for $\alpha > 1$ in E2T8, tilted-jet mode predominated without multi-jet mode within the applied β. In addition, E2T8 showed a wide range of cone-jet mode among the fluids we have covered.

We now compare E4T6 ($\chi = 2.62, \varepsilon' = 14.0$) and E2T8 ($\chi = 2.71$, $\varepsilon' = 9.2$) to see the effect of permittivity on cone-jet formation because they have similar $\chi \sim 2.7$ but different ε' in material properties. For cone-jet formation, at $\alpha = 1$, the cone-jet mode was generated when $(\beta_1 =) 4.4 \leq \beta_{cone-jet} \leq 5.9 (= \beta_2)$ for E4T6 (see Fig. 5-5(c)), and when $(\beta_1 =) 3.8 \leq \beta_{cone-jet} \leq 4.8 (= \beta_2)$ for E2T8 (see Fig. 5-5(d)). In other words, at $\alpha = 1$, the dimensionless voltage $\beta_{cone-jet}$ for cone-jet formation shifted higher as ε' increased when χ was similar. Depending on α, low limit β_1 and high limit β_2 were varied. As a result, the cone-jet modes were generated when $0.5 \leq \alpha \leq 3$ for E4T6 (Fig. 5-5(c)) and for all α in the case of E2T8 (if $T_q/T_h < 1$) (Fig. 5-5(d)). Grey shadow regions in Fig. 5-5 correspond to cone-jet formation. Accordingly, E2T8 showed the most optimized performance for cone-jet mode formation in this study. Based on these

results, we will examine jetting physics in order to understand the nature of the cone-jet mode formation and then suggest evaluating tools for cone-jet stability by characterizing the Taylor cone and jet.

5.3 Jet stability

5.3.1 Charge relaxation length

In Fig. 5-5, the cone-jet mode is the most ideal jetting mode for stable EHD printing, and the surface charge layer should be built up by charge conduction. The thickness of this layer refers to the charge relaxation length, r^* [Chen and Pui (1997)] and it is defined as follows,

$$r^* = (Q_s T_q)^{1/3} \tag{5-2}$$

where Q_s is the supplied flow rate and T_q is the charge relaxation time. This supports that the charge conduction is determined by the supplied flow rate Q_s and charge relaxation time ~$\varepsilon_0 \varepsilon' / K$. The charge relaxation length r^* which was calculated from eq. (5-2) is shown in Fig. 5-6.

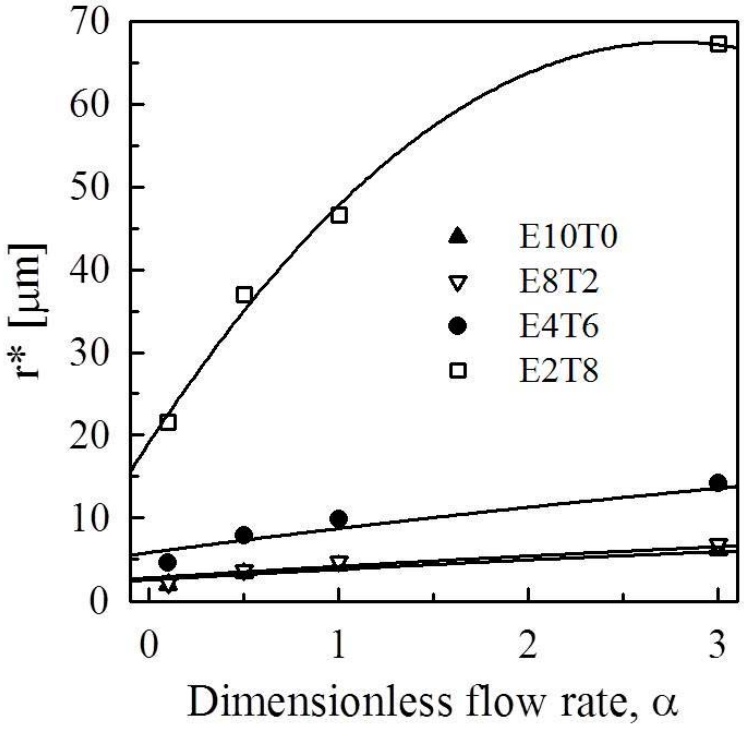

Fig. 5-6 Charge relaxation length r^* as a function of dimensionless flow rate α for fluids: E10T0 ($\chi = 6.05,\ \varepsilon' = 29.1$), E8T2 ($\chi = 4.87,\ \varepsilon' = 22.8$), E4T6 ($\chi = 2.62,\ \varepsilon' = 14.0$) and E2T8 ($\chi = 2.71,\ \varepsilon' = 9.2$).

There is a significant difference in r^* between the fluids E4T6 ($\chi = 2.62$, $\varepsilon' = 14.0$) and E2T8 ($\chi = 2.71$, $\varepsilon' = 9.2$) due to different ε' in spite of similar $\chi \sim 2.7$. E4T6 had thinner (smaller r^*) and denser (higher ε') charge layer than E2T8, thus in order to strip off the generated r^* of E4T6 by accelerating the charges (composed of ions) and surrounding fluids towards the cone apex, relatively large electric potential should be applied. This result supports that E4T6 had larger β_1 (low limit β for cone-jet formation) than E2T8 in Fig. 5-5. In other words, r^* which is a thickness of surface charge layer generated by charge conduction and the applied voltage $\beta_{cone-jet}$ that strips off the charge layer are decisive parameters for cone-jet stability.

5.3.2 Characterization of cone-jet mode

We investigated cone angle and jet diameter in cone-jet mode with respect to the processing conditions and the fluid properties. In this study, d_{jet} was defined as the jet diameter at a distance of $500\,\mu$m from nozzle exit and θ was designated as the semi-cone angle of cone apex (see Fig. 5-7). The cone-jet images for E4T6 ($\chi = 2.62$, $\varepsilon' = 14.0$) and E2T8 ($\chi = 2.71$, $\varepsilon' = 9.2$) with respect to processing parameters, α and β, are given in Fig. 5-8(a) and Fig. 5-8(b).

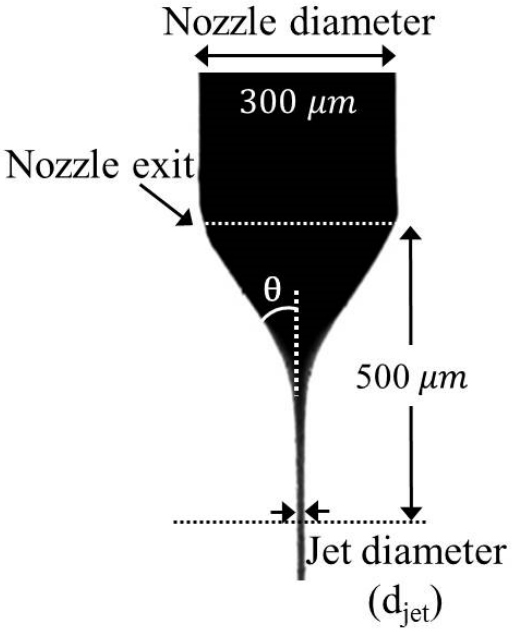

Fig. 5-7 Definition of jet diameter d_{jet} and semi-cone angle θ in cone-jet mode.

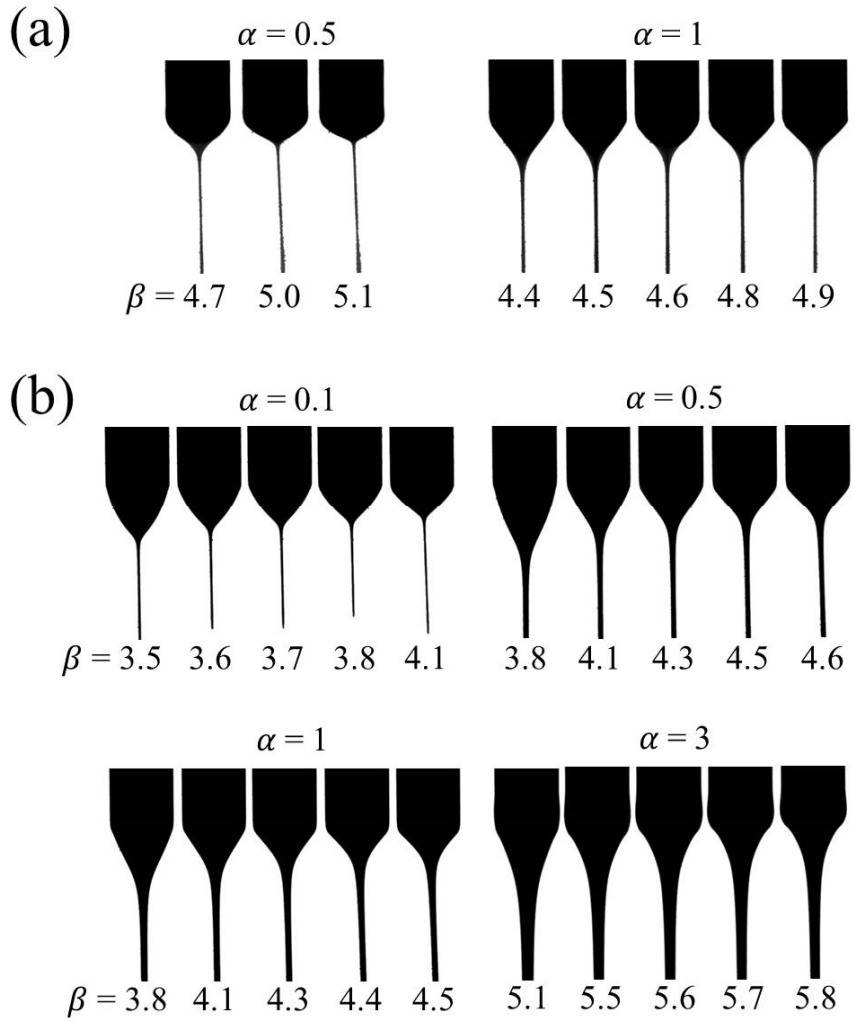

Fig. 5-8 Cone-jet images for (a) E4T6 ($\chi = 2.62,\ \varepsilon' = 14.0$) and (b) E2T8 ($\chi = 2.71,\ \varepsilon' = 9.2$) with respect to α and β.

The jet diameter d_{jet} was analyzed based on the images in Fig. 5-8. While d_{jet} was increased with α and d_{jet} was decreased with β for E4T6 and E2T8 (see Fig. 5-9 – top). In addition, the normalized d_{jet} with charge relaxation length r^* was close to unity ($d_{jet}/r^* \sim 1$) (see Fig. 5-9 – bottom). So d_{jet} can be predicted and the printed pattern with fine resolution can be obtained by tuning the material properties once r^* is known. Taylor angle θ_T is known to be 49.3^o [Taylor (1964), Li (2006)]. This was theoretically calculated from the balance of capillary and electric pressures under no fluid motion (zero hydrostatic pressure). However practical system is put under flow/electric fields, so that it has discrepancy from the theoretical one. The semi-cone angle θ increased with β (see Fig. 5-10 – top), and the normalized θ with θ_T approached to one ($\theta/\theta_T \sim 1$) with a little variation (see Fig. 5-10 – bottom).

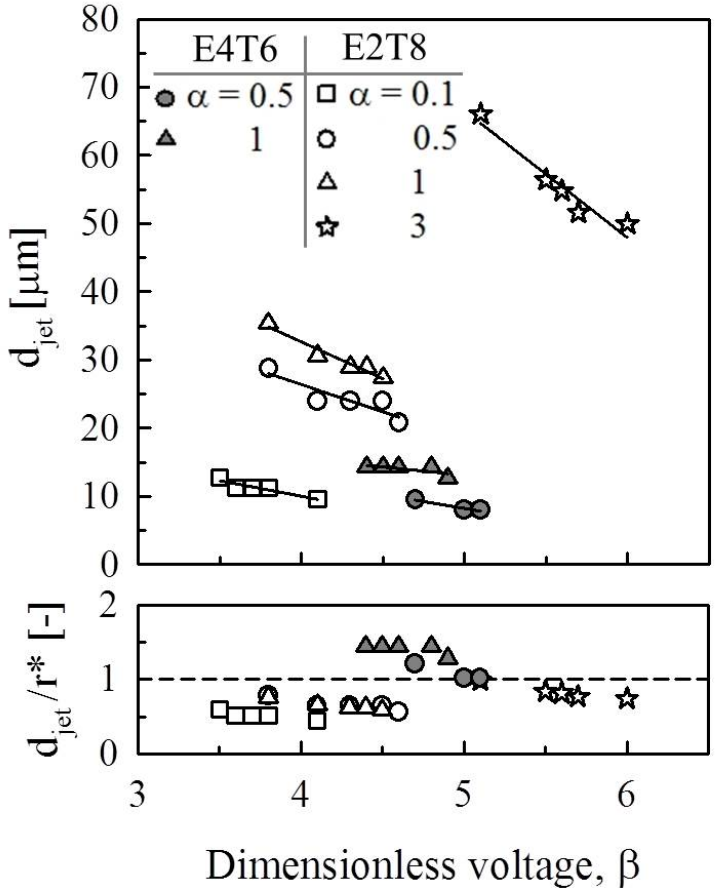

Fig. 5-9 Jet diameter d_{jet} (top) and normalized jet diameter with charge relaxation length r^* as a function of dimensionless voltage β (bottom) for E4T6 ($\chi = 2.62,\ \varepsilon' = 14.0$) and E2T8 ($\chi = 2.71,\ \varepsilon' = 9.2$).

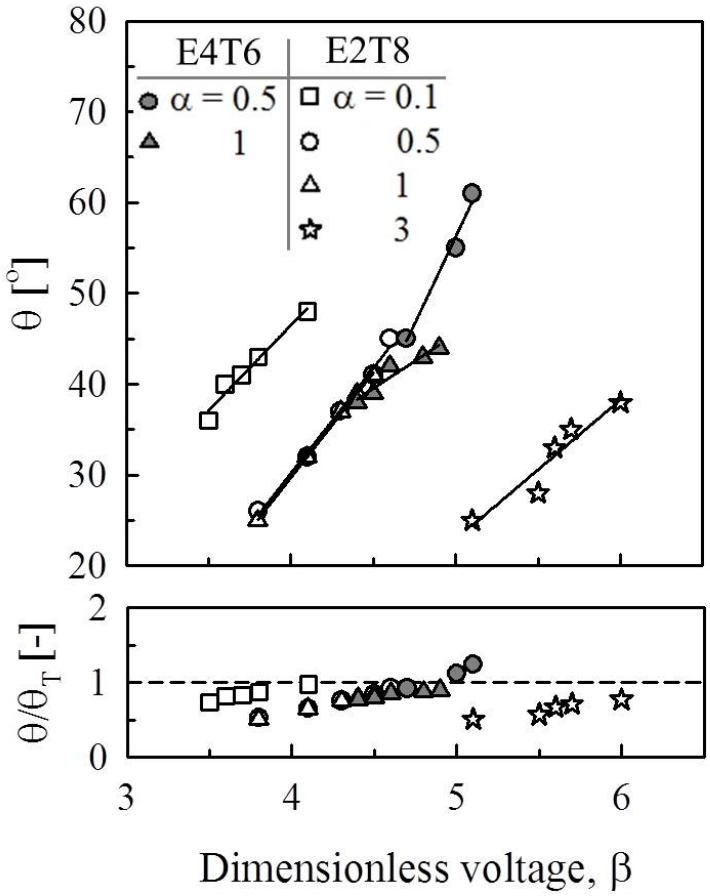

Fig. 5-10 Semi-cone angle θ (top) and normalized semi-cone angle with Taylor angle θ_T (bottom) for E4T6 ($\chi = 2.62,\ \varepsilon' = 14.0$) and E2T8 ($\chi = 2.71,\ \varepsilon' = 9.2$).

5.3.3 Ratio of electrostatic forces (Numerical simulation)

We conducted numerical simulation in order to estimate the electric normal and tangential forces ($F_{E,n}, F_{E,t}$), and compared the results with experiments. The charge transport originates from both conduction by electric field and convection by flow field while the cone angle, the electric field and the surface stress change simultaneously depending on the electric potential. To take all these factors into account, we have to solve the conservation equations of momentum and the electrodynamic equations at the same time. In this simulation, only the effect of electric field was investigated by using the information on geometry which was obtained experimentally from the given potential difference.

To calculate the electric field in Fig. 5-11(a), we solved the following equations by using commercial software COMSOL Multiphysics (COMSOL 4.2, Comsol Inc., U.S.A.):

$$\mathbf{E} = -\nabla\emptyset \tag{5-3a}$$

$$\mathbf{D} = \varepsilon\mathbf{E} \tag{5-3b}$$

$$\nabla \cdot \mathbf{D} = \rho \tag{5-3c}$$

where $\mathbf{E}$ is the electric field, $\emptyset$ is the electric potential, ε is the

permittivity and ρ is the charge density. We refined mesh in the cone part and the total number of elements was about 12,000. The simulation domain in r-direction was set to 10 times of the nozzle radius, and only a part of it is shown in Fig. 5-11(b). The permittivity was 9.2 for E2T8 and 14.0 for E4T6 in fluid phase (green) and 1.0 in gas phase (blue), respectively.

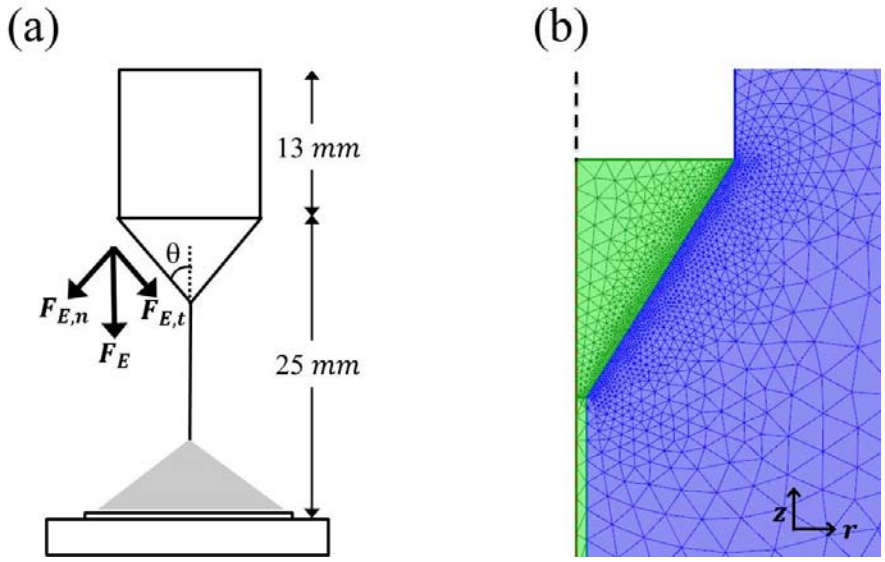

Fig. 5-11 (a) Simulation domain. The nozzle size and the length of nozzle head are 300 μm and 13 mm, repectively. The distance between nozzle and counter electrode was set to be 25 mm. (b) Mesh: green and blue colors correspond to fluid and gas phase, respectively.

The simulation was performed in cylindrical coordinate; E_r and E_Z were obtained at the surface of the cone. They were transformed to normal component E_n and tangential component E_t with the information of cone angle, and then the electric stresses due to the electric field at the surface were obtained as follows [Hayati *et al*. (1987)].

$$\tau_{E,n} = \frac{1}{2}\varepsilon_0 {E_n}^2 + \frac{1}{2}(\varepsilon - \varepsilon_0){E_t}^2 \tag{5-4a}$$

$$\tau_{E,t} = \varepsilon_0 E_t E_n \tag{5-4b}$$

The forces acting on the surface was calculated by integrating the electric stress over the free surface,

$$F_{E,n(t)} = \int \tau_{E,n(t)} dA \tag{5-5}$$

where A is the area of the cone.

Here, $F_{E,n}$ is the normal component of the electrostatic force which tends to destabilize the cone-jet by acting on the meniscus outwards, and $F_{E,t}$ is the tangential component of the electrostatic force which tends to stabilize the cone-jet by acting along the meniscus towards the cone apex. Therefore, the ratio of two forces $F_{E,n}/F_{E,t}$ can be used as an evaluation parameter of cone-jet stability. As $F_{E,n}/F_{E,t}$ becomes larger, the cone-jet becomes less stable, whereas when $F_{E,n}/F_{E,t}$ becomes smaller, the cone-jet tends to be stable. In addition, as the slope of $F_{E,n}/F_{E,t}$ with respect to the

dimensionless voltage β becomes larger, the cone-jet may proceed to an unstable jet more rapidly. Compared with the experimental results in Fig. 5-3, the cone-jet mode will be transformed to tilted, twin and multi-jet mode as β increases. The tendency of $F_{E,n}/F_{E,t}$ and the slope of E2T8 ($\chi = 2.71$, $\varepsilon' = 9.2$) and E4T6 ($\chi = 2.62$, $\varepsilon' = 14.0$) with respect to α and β are given in Fig. 5-13.

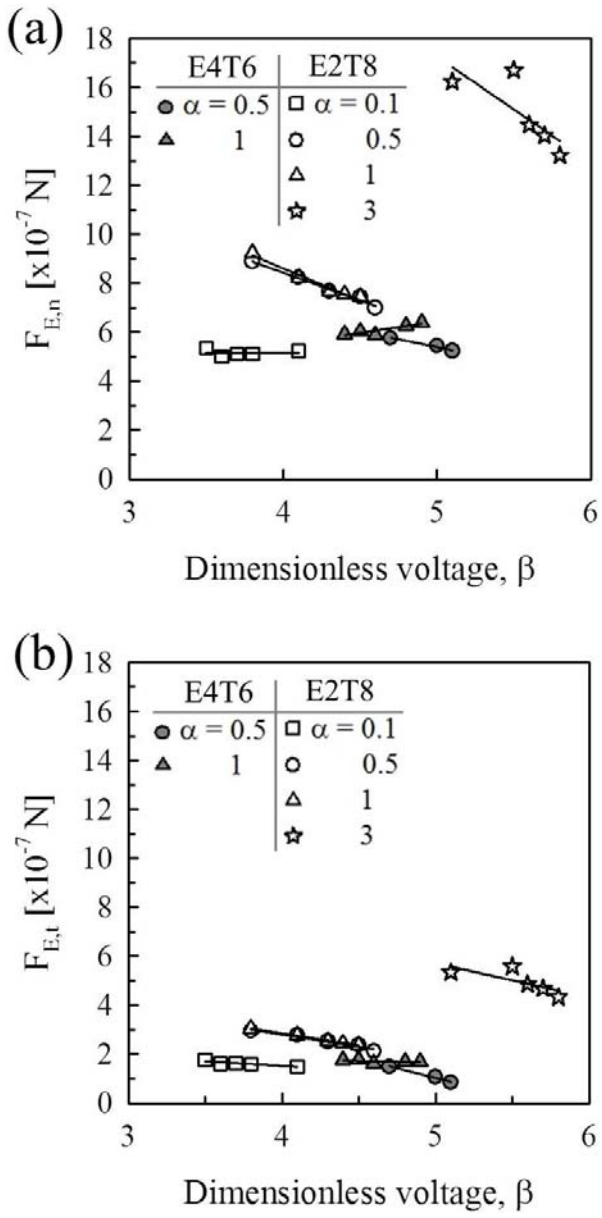

Fig. 5-12 (a) Electric normal force $F_{E,n}$ and (b) electric tangential force $F_{E,t}$ for E4T6 ($\chi = 2.62,\ \varepsilon' = 14.0$) and E2T8 ($\chi = 2.71,\ \varepsilon' = 9.2$), with respect to α and β.

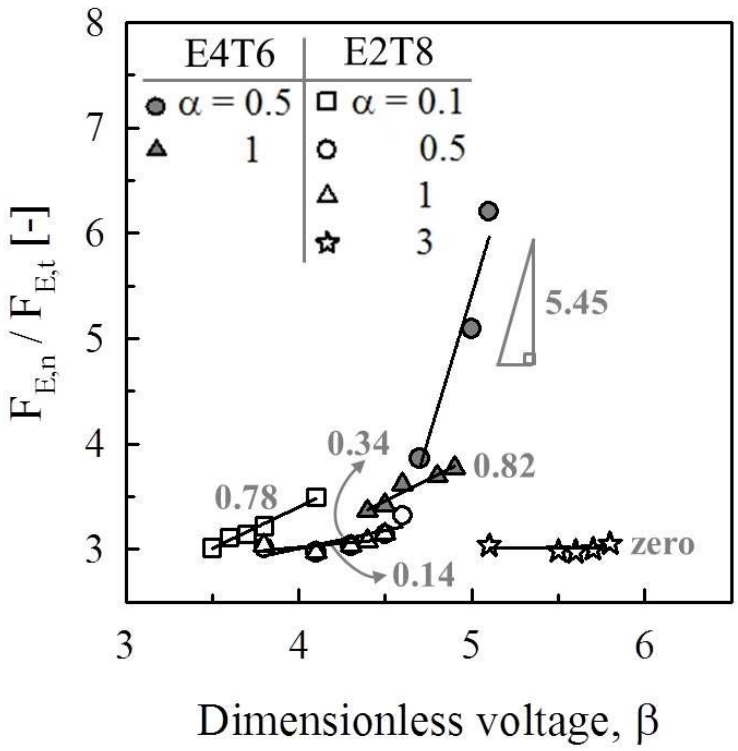

Fig. 5-13 $F_{E,n}/F_{E,t}$, the ratio of electric normal force $F_{E,n}$ and electric tangential force $F_{E,t}$ for E4T6 ($\chi = 2.62,\ \varepsilon' = 14.0$) and E2T8 ($\chi = 2.71,\ \varepsilon' = 9.2$), with respect to α and β. The slopes of $F_{E,n}/F_{E,t}$ are displayed in the graph.

In Fig. 5-13 shows that the ratio between electric normal force $F_{E,n}$ and electric tangential force $F_{E,t}$ was larger than three ($F_{E,n}/F_{E,t} \geq 3$) for both E4T6 and E2T8. When calculated from the paper of Hayati *et al*. (1987), it turned out that $F_{E,n}$ was almost 3.7 times larger than $F_{E,t}$ ($F_{E,n}/F_{E,t} > 3.7$) independent of flow rate. The slope of $F_{E,n}/F_{E,t}$ was 5.45 for E4T6 and 0.34 for E2T8 at $\alpha = 0.5$, and 0.82 for E4T6 and 0.14 for E2T8 at $\alpha = 1$. At the same α, the slope of E4T6 was larger than that of E2T8 because larger ε' tends to promote unstable jet more rapidly (when χ is similar). On the other hand, for E2T8 at $\alpha = 3$, there was no change in $F_{E,n}/F_{E,t}$, which means that β contributes to the jet acceleration rather than to the jet stability at large flow rate. The ratio of electrostatic forces can be a new evaluating parameter for cone-jet stability.

Chapter 6. Conclusions

Firstly, in drop-on-demand piezo inkjet printing (PIJ), the drop jettability during inkjet printing has been investigated for zinc oxide (ZnO) particulate suspensions. In analogy to the approach for judging the drop formation properties of Newtonian fluids the dimensionless number Z as an inverse Ohnesorge number, Oh^{-1} was introduced to the range of printability in dependence of viscosity, surface tension, and density of the inks. For the inkjet printing setup used here, we could demonstrate that jetting was possible without any problem for Newtonian fluids as long as $2.5 < Z < 26$, but in the identical range, nonjetting occurred due to nozzle clogging for certain colloidal ZnO suspensions, and this is attributed to flow-induced aggregation in the contraction zone at the nozzle exit.

This flow-induced aggregation phenomenon was further investigated using a so-called ring-slit device. This device allows for simultaneous formation and detection of aggregates in strongly converging flow fields and is operated here under similar conditions as the inkjet printer regarding flow velocity v_x and slit height H or nozzle diameter D.

We could show that the pressure increase during extrusion of the suspension through the ring-slit is correlated to the nozzle clogging observed in inkjet printing. Our experiments suggest that the flow-induced aggregation is promoted by a small fraction of micrometer-sized aggregates acting as nuclei for heterocoagulation with the nanoscale suspension particles in the contraction zone. Especially, the aggregates in the size range between 1 and 6 μm are decisive imparting nozzle clogging thereby preventing proper inkjet printing, even though the size of these aggregates is smaller than the size of the nozzle cross-section. The relative volume fraction of aggregates, $\varphi_{\mathrm{aggregates}}/\varphi_{\mathrm{initial}} \geq 1\ \mu$m, should not exceed 500 ppm, and their total number should be below 7×10^5/mL in order to avoid nozzle clogging. Flow-induced aggregation can also be suppressed by appropriate stabilization of the nanoparticles, but this is often not achievable without impairing the electric performance of the printed structure. From a processing or printing head design perspective, clogging probability can be reduced either by applying a higher driving voltage, which corresponds to a higher flow rate, or by optimizing the contraction zone such that the exposure time of the ink to the elongational flow field is reduced. The former results in a break-up of existing or previously formed aggregates; the latter corresponds to a lower probability of aggregate formation.

Finally, this study clearly reveals that besides the classical inverse Ohnesorge number criterion additional colloidal stability parameters have to be considered in order to optimize suspension based printing inks for inkjet printing purposes and that the printing process parameters and nozzle design may have to be adjusted in order to establish this promising technology for low cost manufacturing of electronic devices.

Secondly, in electrohydrodynamic inkjet printing (EHD), with the Buckingham pi theorem, six dimensionless numbers $D_1 \sim D_6 = (T_q/T_h, \chi, \varepsilon', d/L, \alpha, \beta)$ governing EHD printing system were systemized, and jetting maps were drawn for ethanol/terpineol mixtures based on these parameters. For classical EHD printing system of $T_q/T_h < 1$, at $\alpha = 1$, the cone-jet mode was generated at $4.4 \leq \beta_{cone-jet} \leq 5.9$ for E4T6 and $3.8 \leq \beta_{cone-jet} \leq 4.8$ for E2T8, respectively, which have similar $\chi \sim 2.7$ (the ratio of characteristic velocity of the bulk fluid and propagation velocity of the perturbation by viscous diffusion) but different ε' (fluid permittivity). Since E4T6 has thinner (smaller r^*) and denser (higher ε') charge layer than E2T8, to strip off the generated r^* of E4T6 by accelerating charges and surrounding fluids towards the cone apex, relatively large electric potential should be applied. In the cone-jet mode, the normalized d_{jet} with r^* approached to unity, so it is highly probable that d_{jet} can be predicted

from the information on r^*, and it is possible to optimize the value by adjusting the fluid properties. In addition, the normalized θ with θ_T approached to one with a little variation. By numerical simulation, we could suggest the ratio of two electrostatic forces, $F_{E,n}/F_{E,t}$ as an evaluation parameter for cone-jet stability. The smaller the ratio, the more the cone-jet tends to be stable. In addition, as the slope of the ratio with respect to β becomes larger, the cone-jet may proceed to an unstable jet more rapidly. These were matched well with the experimental results.

The setup of the dimensionless numbers and the evaluating tools of cone-jet stability are the systematic and effective methods to obtain the stable Taylor cone of cone-jet mode as the targeted jetting mode, and the control of inks with optimized experimental parameters will contribute to better design with improved jetting performance in EHD inkjet printing.

Nomenclature

ρ : Density $[Kg\ m^{-3}]$

γ : Surface tension $[N\ m^{-1}]$

d : Nozzle diameter $[\mu m]$

η : Viscosity $[Pa \cdot s]$

η_{app} : Apparent viscosity $[Pa \cdot s]$

$\dot{\gamma}$: Shear rate $[s^{-1}]$

$\dot{\gamma}_{\text{app}}$: Apparent shear rate $[s^{-1}]$

$\dot{\gamma}_{\text{wall}}$: Wall shear rate $[s^{-1}]$

τ_{app} : Apparent shear stress $[Pa]$

$\langle v_x \rangle$: Average drop velocity $[m\ s^{-1}]$

Z $(= \text{Oh}^{-1})$: Inverse Ohnesorge number

Re : Reynolds number

We : Weber number

Pe : Péclet number

G^* : Complex shear modulus $[Pa]$

G' : Storage modulus $[Pa]$

G'' : Loss modulus $[Pa]$

ε_0 : Permittivity of free space $[F\ m^{-1}]$

ε' : Permittivity of fluid

K : Conductivity $[S\ m^{-1}]$

T_h : Hydrodynamic time $[s]$

T_q : Charge relaxation time $[s]$

L : Distance of nozzle and counter-electrode $[m]$

χ : Dimensionless characteristic velocity

α : Dimensionless flow rate

Q_s : Supplied flow rate $[m^3\ s^{-1}]$

Q_c : Critical flow rate $[m^3\ s^{-1}]$

β : Dimensionless voltage

V_a : Applied voltage $[V]$

V_c : Critical voltage $[V]$

$\boldsymbol{E}$: Electric field $[V/m]$

$\emptyset$: Electric potential $[V]$

$\tau_{E,n}$: Electric normal stress $[Pa]$

$\tau_{E,t}$: Electric tangential stress $[Pa]$

F_E : Electrostatic force $[N]$

$F_{E,n}$: Electric normal force $[N]$

$F_{E,t}$: Electric tangential force $[N]$

r^* : Charge relaxation length $[m]$

d_{jet} : Jet diameter $[m]$

θ_T : Taylor angle [rad or ^{o}]

θ : Semi-cone angle [rad or ^{o}]

$[M]$: Mass

[L] : Length

$[T]$: Time

$[V]$: Voltage

Bibliography

In alphabetical order by first author,

Ashgriz, N. Handbook of Atomization and Sprays, theory and applications. Springer, New York, **2011**.

Barrero, A.; Ganan-Calvo, A. M.; Davila, J.; Palacios, A.; Gomez-Gonzalez, E. The role of the electrical conductivity and viscosity on the motions inside Taylor cones. J Electrostat 47: 13-26, **1999**.

Beulen, B.; de Jong, J.; Reinten, H.; van den Berg, M.; Wijshoff, H.; van Dongen, R. Flows on the nozzle plate of an inkjet printhead. Exp. Fluids, 42, 217−224, **2007**.

Bubel, S.; Nikolova, D.; Mechau, N.; Hahn., H. Influence of stabilizers in ZnO nanodispersions on field-effect transistor device performance. J. Appl. Phys., 105, 064514, **2009**.

Cardinal, C. M.; Jung, Y. D.; Ahn, K. H.; Francis, L. F. Drying regime maps for particulate coatings. AIChE J., 56, 2769−2780, **2010**.

Chen, D. R.; Pui, D. Y. H. Experimental investigation of scaling laws for electrospraying: Dielectric constant effect. Aerosol Sci Tech 27:

367-380, **1997**.

Choi, K. H.; Muhammad, N. M.; Dang, H. W, Lee, A.; Hwang, J. S.; Nam, J. W.; Ryu, B. H. Electrospray deposition of thin copper-indium-diselenide films. Int J Mater Res 102: 1252-1260, **2011**.

Cibis, D.; Kru¨ger, K. System analysis of a DoD print head for direct writing of conductive circuits. Int. J. Appl. Ceram. Technol., 4, 428−435, **2007**.

Cloupeau, M.; Prunetfoch, B. Electrostatic Spraying of Liquids in Cone-Jet Mode. J Electrostat 22: 135-159, **1989**.

Degen, A.; Kosec, M. Effect of pH and impurities on the surface charge of zinc oxide in aqueous solution. J. Eur. Ceram. Soc., 20, 667−673, **2000**.

de Jong, J.; de Bruin, G.; Reinten, H.; van den Berg, M.; Wijshoff, H.; Versluis, M.; Lohse, D. Air entrapment in piezo-driven inkjet printheads. J. Acoust. Soc. Am., 120, 1257−1265, **2006**.

Deitzel, J. M.; Kleinmeyer, J. D.; Hirvonen, J. K.; Tan N. C. B. Controlled deposition of electrospun poly(ethylene oxide) fibers. Polymer 42: 8163-8170, **2001**.

Dasgupta, S.; Gottschalk, S.; Kruk, R.; Hahn, H. A nanoparticulate indium tin oxide field-effect transistor with solid electrolyte gating.

Nanotechnology, 435203, **2008**.

Edirisinghe, M. J.; Jayasinghe, S. N. Electrohydrodynamic Atomization of a Concentrated Nano-Suspension. Int J Appl Ceram Tec 1: 140-145, **2004**.

Ekemen, Z.; Ahmad, Z.; Stride, E.; Kaplan, D. L.; Edirisinghe, M. Electrohydrodynamic Bubbling: An Alternative route to Fabricate Porous Structures of Silk Fibroin Based Materials. Biomacromolecules, in press, **2013**.

Ettl, R.; Schadler, V.; Willenbacher, N. Runnability and flow-induced aggregation of paper coating suspensions. Nord. Pulp Pap. Res. J., 15, 509−514, **2000**.

Fakhfouri, V.; Mermoud, G.; Kim, J. Y.; Martinoli, A.; Brugger, J. Drop-on-demand inkjet printing of SU-8 polymer. Micro Nanosyst., 1, 63−67, **2009**.

Ganan-Calvo, A. M. Cone-jet analytical extension of Taylor's electrostatic solution and the asymptotic universal scaling laws in electrospraying. Phys Rev Lett 79: 217-220, **1997a**.

Ganan-Calvo, A. M. On the theory of electrohydrodynamically driven capillary jets. J Fluid Mech 335: 165-188, **1997b**.

Ganan-Calvo, A. M.; Davila, J.; Barrero, A. Current and droplet size in the

electrospraying of liquids. Scaling laws. J Aerosol Sci 28: 249-275, **1997**.

Georgieva, K.; Dijkstra, D. J.; Fricke, H.; Willenbacher, N. Clogging of microchannels by nano-particles due to hetero-coagulation in elongational flow. J. Colloid Interface Sci., 352, 265−277, **2010**.

Gomez-Estaca, J.; Balaguer, M. P.; Gavara, R.; Hernandez-Munoz, P. Formation of zein nanoparticles by electrohydrodynamic atomization: Effect of the main processing variables and suitability for encapsulating the food coloring and active ingredient curcumin. Food Hydrocolloid 28: 82-91, **2012**.

Grigoriev, D. A.; Edirisinghe, M.; Bao, X. Deposition of fine silicon carbide relics by electrostatic atomization of a polymeric precursor. J Mater Res 17: 487-491, **2002**.

Habas, S. E.; Platt, H. A. S.; van Hest, M. F. A. M.; Ginley, D. S. Low-cost inorganic solar cells: From ink to printed device. Chem. Rev., 110, 6571−6594, **2010**.

Hartman, R. P. A.; Brunner, D. J.; Camelot, D. M. A.; Marijnissen, J. C. M.; Scarlett, B. Electrohydrodynamic atomization in the cone-jet mode physical modeling of the liquid cone and jet. J Aerosol Sci 30: 823-849, **1999**.

Hayati, I.; Bailey, A. I.; Tadros, T. F. Mechanism of Stable Jet Formation in Electrohydrodynamic Atomization. Nature 319: 41-43, **1986**.

Hayati, I.; Bailey, A. I.; Tadros, T. F. Investigations into the Mechanisms of Electrohydrodynamic Spraying of Liquids .1. Effect of Electric-Field and the Environment on Pendant Drops and Factors Affecting the Formation of Stable Jets and Atomization. J Colloid Interf Sci 117: 205-221, **1987a**.

Hayati, I.; Bailey, A. I.; Tadros, T. F. Investigations into the mechanism of electrohydrodynamic spraying of liquids: II. Mechanism of stable jet formation and electrical forces acting on a liquid cone. J Colloid Interf Sci 117: 222-230, **1987b**.

Hommer, H. Interaction of polycarboxylate ether with silica fume. J. Eur. Ceram. Soc., 29, 1847－1853, **2009**.

Kim, S.; Kim, J. H.; Ahn, K. H.; Lee, S. J. Rheological perspectives of industrial coating process. Korea-Aust. Rheol. J., 21, 83－89, **2009**.

Jang, D.; Kim, D.; Moon, J. Influence of fluid physical properties on ink-jet printability. Langmuir, 25, 2629－2635, **2009**.

Jaworek, A.; Krupa, A. Classification of the modes of EHD spraying. J Aerosol Sci 30: 873-893, **1999**.

Jayasinghe, S. N.; Edirisinghe, M. J. Effect of viscosity on the size of relics

produced by electrostatic atomization. J Aerosol Sci 33: 1379-1388, **2002a**.

Jayasinghe, S. N.; Edirisinghe, M. J. Obtaining fine droplet relics by electrostatic atomization of viscous liquids. J Mater Sci Lett 21: 371-373, **2002b**.

Jayasinghe, S. N.; Edirisinghe, M. J. Electric-field driven jetting from dielectric liquids. Appl Phys Lett 85: 4243-4245, **2004a**.

Jayasinghe, S. N.; Edirisinghe, M. J. Electrically forced jets and microthreads of high viscosity dielectric liquids. J Aerosol Sci 35: 233-243, **2004b**.

Jeong, S.; Kim, D.; Moon, J. Ink-Jet-printed organic−inorganic hybrid dielectrics for organic thin-film transistors. J. Phys. Chem. C, 112, 5245−5249, **2008**.

Jo, B. W.; Lee, A.; Ahn, K. H.; Lee, S. J. Evaluation of jet performance in drop-on-demand (DOD) inkjet printing. Korean J. Chem. Eng., 26, 339−348, **2009**.

Joffre, G. H.; Cloupeau, M. Characteristic forms of electrified menisci emitting charges. J Electrostat 18: 147-161, **1986**.

Kim, H. S.; Lee, D. Y.; Park, J. H.; Kim, J. H.; Hwang, J. H.; Jung, H. I. Optimization of electrohydrodynamic writing technique to print

collagen. Exp Techniques Experimental Techniques 31: 15-19, **2007**.

Kwon, K. S.; Kim, W. A waveform design method for high-speed inkjet printing based on self-sensing measurement. Sens. Actuators A, 140, 75－83, **2007**.

Kwon, K. S. Waveform design methods for piezo inkjet dispensers based on measured meniscus motion. J. Microelectromech. Syst., 18, 1118－1125, **2009**.

Lee, A.; Sudau, K.; Ahn, K. H.; Lee, S. J.; Willenbacher, N. Optimization of Experimental Parameters to Suppress Nozzle Clogging in Inkjet Printing. Ind Eng Chem Res 51(40): 13195-13204, **2012**.

Li, J. L. On the meniscus deformation when the pulsed voltage is applied. J Electrostat 64: 44-52, **2006**.

Luo, C. J.; Loh, S.; Stride, E.; Edirisinghe, M. Electrospraying and Electrospinning of Chocolate Suspensions. Food Bioprocess Tech 5: 2285-2300, **2012**.

Maki, K. L.; Kumar, S. Fast evaporation of spreading droplets of colloidal suspensions. Langmuir, 27, 11347－11363, **2011**.

Marmottant, P.; Hilgenfeldt, S. Controlled vesicle deformation and lysis by single oscillating bubbles. Nature, 423, 153－156, **2003**.

Mathews, N.; Lam, Y. M.; Mhaisalkar, S. G.; Grimadale, A. C. Printing

materials for electronic devices. Int. J. Mat. Res., 101, 236−250, **2010**.

McKinley, G. H. Dimensionless groups for understanding free surface flows of complex fluids. Rheol. Bull., 74 (2), 6−10, **2005**.

Mechau, N.; Bubel, S.; Nikolova, D.; Hahn, H. Influence of stabilizers in ZnO nano-dispersions on the performance of solutionprocessed FETs. Phys. Status Solidi A, 207, 1684−1688, **2010**.

Mestel, A. J. The electrohydrodynamic cone-jet at high reynolds number. J Aerosol Sci 25: 1037-1047, **1994**.

Muhammad, N. M.; Sundharam, S.; Dang, HW.; Lee, A.; Ryu, BH.; Choi, KH. CIS layer deposition through electrospray process for solar cell fabrication. Curr Appl Phys 11: S68-S75, **2011**.

Okamura, K.; Mechau, N.; Nikolova, D.; Hahn, H. Influence of interface roughness on the performance of nanoparticulate zinc oxide field-effect transistors. Appl. Phys. Lett., 93, 083105, **2008**.

Okamura, K.; Nikolova, D.; Mechau, N.; Hahn, H. Polymer stabilized ZnO nanoparticles for low-temperature and solution processed field-effect transistors. J. Mater. Chem., 20, 5651−5658, **2010**.

Park, J. U.; Hardy, M.; Kang, S. J.; Barton, K.; Adair, K.; Mukhopadhyay, D.; Lee, C. Y.; Strano, M. S.; Alleyne, A. G.; Georgiadis, J. G.; Ferreira,

P. M.; Rogers, J. A. High-resolution electrohydrodynamic jet printing. Nat Mater 6: 782-789, **2007**.

Park, J. U.; Lee, J. H.; Paik, U.; Lu Y.; Rogers, J. A. Nanoscale Patterns of Oligonucleotides Formed by Electrohydrodynamic Jet Printing with Applications in Biosensing and Nanomaterials Assembly. Nano Lett 8: 4210-4216, **2008**.

Park, S. E.; Hwang, J. Y.; Kim, K.; Jung, B.; Kim, W.; Hwang, J. Spray deposition of electrohydrodynamically atomized polymer mixture for active layer fabrication in organic photovoltaics. Sol Energ Mat Sol C 95: 352-356, **2011**.

Perelaer, J.; Smith, P. J.; Wijnen, M. M. P.; van den Bosch, E.; Eckardt, R.; Ketelaars, P. H. J. M.; Schubert, U. S. Droplet tailoring using evaporative inkjet printing. Macromol. Chem. Phys., 210, 387－393, **2009**.

Perelaer, J.; Smith, P. J.; Mager, D.; Soltman, D.; Volkman, S. K.; Subramanian, V.; Korvink, J. G.; Schubert, U. S. Printed electronics: the challenges involved in printing devices, interconnects, and contacts based on inorganic materials. J. Mater. Chem., 20, 8446－8453, **2010**.

Pilch, M.; Erdman, C. A. Use of Breakup Time Data and Velocity History

Data to Predict the Maximum Size of Stable Fragments for Acceleration-Induced Breakup of a Liquid-Drop. Int. J. Multiphase Flow, 13, 741−757, **1987**.

Ramachandran, V.; Fogler, H. S. Plugging by hydrodynamic bridging during flow of stable colloidal particles within cylindrical pores. J. Fluid Mech., 385, 129−156, **1999**.

Reis, N.; Ainsley, C.; Derby, B. Ink-jet delivery of particle suspensions by piezoelectric droplet ejectors. J. Appl. Phys., 97, 094903, **2005**.

Remsen, E. E.; Anjur, S.; Boldridge, D.; Kamiti, M.; Li, S.; Johns, T.; Dowell, C.; Kasthurirangan, J.; Feeney, P. Analysis of large particle count in fumed silica slurries and its correlation with scratch defects generated by CMP. J. Electrochem. Soc., 153, G453−G461, **2006**.

Shakhnovich, A.; Belmont, J. The Chemistry of Inkjet Inks. Part II: Formulation and Materials for Inkjet Inks; Magdassi, S., Ed.; World Scientific, pp 101−122. http://www.worldscientific.com/worldscibooks/10.1142/6869# t = t o c, DOI: 10.1142/9789812818225_0006, **2009**.

Shin, Y. M.; Hohman, M. M.; Brenner, M. P.; Rutledge, G. C. Experimental characterization of electrospinning: the electrically forced jet and instabilities. Polymer 42: 9955-9967, **2001**.

Sirringhaus, H.; Kawase, T.; Friend, R. H.; Shimoda, T.; Inbasekaran, M.; Wu, W.; Woo, E. P. High-resolution inkjet printing of all-polymer transistor circuits. Science, 290, 2123−2126, **2000**.

Sis, H.; Birinci, M. Effect of nonionic and ionic surfactants on zeta potential and dispersion properties of carbon black powders. Colloids Surf., A, 341, 60−67, **2009**.

Sun, Y.; Rogers, J. A. A. Inorganic semiconductors for flexible electronics. Adv. Mater., 19, 1897−1916, **2007**.

Tafreshi, H. V.; Pourdeyhimi, B. The effects of nozzle geometry on waterjet breakup at high Reynolds numbers. Exp. Fluids, 35, 364−371, **2003**.

Tai, J. Y.; Gan, H. Y.; Liang, Y. N.; Lok, B. K. Control of droplet formation in inkjet printing using Ohnesorge number category: Materials and processes. In Proceedings of the 10th Electronics Packaging Technology Conference (ECTC2008), Singapore, pp 761−766, **2008**.

Taylor, G. Disintegration of Water Drops in an Electric Field. P Roy Soc Lond A Mat 280: 383-397, **1964**.

Tekin, E.; Smith, P. J.; Schubert, U. S. Inkjet printing as a deposition and patterning tool for polymers and inorganic particles. Soft Matter, 4,

703−713, **2008**.

Theron, S. A.; Zussman, E.; Yarin, A. L. Experimental investigation of the governing parameters in the electrospinning of polymer solutions. Polymer 45: 2017-2030, **2004**.

Tsai, B.; Carvalho, M. S.; Kumar, S. Leveling of thin films of colloidal suspensions. J. Colloid Interface Sci., 343, 306−313, **2010**.

Tuladhar, T. R.; Mackley, M. R. Filament stretching rheometry and break-up behavior of low viscosity polymer solutions and inkjet fluids. J. Non-Newtonian Fluid Mech., 148, 97−108, **2008**.

Vadillo, D. C.; Tuladhar, T. R.; Mulji, A. C.; Jung, S.; Hoath, S. D.; Mackley, M. R. Evaluation of the inkjet fluid's performance using the "Cambridge Trimaster" filament stretch and break-up device. J. Rheol., 54, 261−282, **2010a**.

Vadillo, D. C.; Tuladhar, T. R.; Mulji, A. C.; Mackley, M. R. The rheological characterization of linear viscoelasticity for ink jet fluids using piezo axial vibrator and torsion resonator rheometers. J. Rheol., 54, 781−795, **2010b**.

Wang, X.; Carr, W. W.; Bucknall, D. G.; Morris, J. F. Drop-on demand drop formation of colloidal suspensions. Int. J. Multiphase Flow, 38, 17−

26, **2012**.

Wyss, H. M.; Blair, D. L.; Morris, J. F.; Stone, H. A.; Weitz, D. A. Mechanism for clogging of microchannels. Phy, Rev. E, 74, 061402, **2006**.

Xie, D. L.; Wu, H.; Zaccone, A.; Braun, L.; Chen, H. Q.; Morbidelli, M. Criticality for shear-induced gelation of charge stabilized colloids. Soft Matter, 6, 2692－2698, **2010**.

Yoon, H.; Woo, J. H.; Ra, YM.; Yoon, S. S.; Kim, H. Y.; Ahn, S. J.; Yun, J. H.; Gwak, J.; Yoon, K. H.; James, S. C. Electrostatic Spray Deposition of Copper–Indium Thin Films. Aerosol Sci Tech 45: 1448-1455, **2011**.

Yudistira, HT.; Nguyen, VD.; Dutta, P.; Byun, D. Flight behavior of charged droplets in electrohydrodynamic inkjet printing. Appl Phys Lett 96: 023503, **2010**.

Zaccone, A.; Wu, H.; Gentili, D.; Morbidelli, M. Theory of activated-rate processes under shear with application to shear-induced aggregation of colloids. Phys. Rev. E, 80, 051404, **2009**.

Zaccone, A.; Gentili, D.; Wu, H.; Morbidelli, M. Shear-induced reaction-limited aggregation kinetics of Brownian particles at arbitrary concentrations. J. Chem. Phys., 132, 134903, **2010**.

Zeleny, J. The electrical discharge from liquid points, and a hydrostatic method of measuring the electric intensity at their surfaces. Phys Rev 3: 69-91, **1914**.

Zeleny, J. Instability of Electrified Liquid Surfaces. Phys Rev 10: 1-6, **1917**.

국문 초록

이아영

학번: 2006-23219

성공적, 기술적 스케일의 잉크젯 프린팅에서 안정한 드랍의 생성은 매우 중요하며, 기초 · 응용 연구의 주된 관심 영역에 있다. 압전 형식의 잉크젯 공정의 경우 역압전 효과에 의해 드랍이 형성된다. 기존 연구는 주로 뉴튼유체, 고분자 용액을 이용하여 수행되었으며, 우리는 입자계 현탁액의 드랍 젯팅을 연구하였다. 일반적으로, 무차원수 $Z = (Oh^{-1})$ 넘버를 이용하여 단일상 유체의 젯팅 여부를 결정한다. 본 연구에서 사용된 잉크젯 프린터에서 뉴튼 유체의 경우 $2.5 < Z < 26$ 범위에서 드랍 젯팅이 가능했던 반면에, 입자계 현탁액 잉크를 사용하였을 경우 유체의 물리적 특성이 젯팅 가능 조건인 동일 Z 범위에 있음에도 불구하고 노즐막힘에 의한 논젯팅 현상이 야기되었다. 이러한 현상을 이해하기 위해 강한 수축 유동

장에서 응집체를 계속적으로 형성, 감지하는 자체 고안된 링슬릿 장비와, 나노입자 현탁액에서 마이크론 응집체의 수와 크기를 정확하게 측정하는 단일입자탐지기술을 이용하였다. 그 결과, 응집체의 크기가 슬릿/노즐 크기보다 현저히 작고 그 농도가 수백 ppm 에 불과하더라도 흐름에 의한 응집현상이 슬릿/노즐 막힘을 야기할 수 있음을 관찰하였으며, 필터링을 통한 응집체의 수와 농도의 조절, 유체의 흐름속도와 수축채널의 각도 등의 공정조건 최적화로부터 흐름에 의한 응집 현상을 완화시킬 수 있음을 확인하였다.

전기장에 의해 야기된 정전기력이 유체의 운동량에 영향을 미치는 전기수력학적 잉크젯 공정에서는 유체의 유변 물성뿐만 아니라 전기적 물성을 고려하여야 한다. 공정 시스템을 지배하는 여섯 개의 무차원수를 디자인하고 무차원수에 따른 젯팅 맵을 도시함으로써, 목표 젯팅 모드인 콘젯모드 영역을 확보하였으며 잉크 물성과 공정 조건에 따른 콘젯 형성 조건을 정량화하였다. 콘 표면에서의 전하층 두께와 무차원수 전압의 상관성에 기반하여 젯 지름을 정량화 · 정규화 하고, 세미콘 각도와 이론적인 테일러 각도를 비교 · 분석 하였다. 또한, 전하를 띤 콘의 표면 방향에서의 힘과 법선 방향에서의 힘의 비를 수치모사 하였다. 이는 콘젯 안정성 정도를 평가

하는 파라미터로서 제안되었으며 힘의 비가 작아질수록 콘젯은 더욱 안정해지는 결과를 보여주었다.

본 연구는 압전- 그리고 전기수력학적 잉크젯 공정의 최적화된 디자인을 위해 각 공정 특성에 따른 파라미터를 제시하고 젯팅 안정성을 확보하기에 유용한 방법론을 제안하였다. 이러한 방법론은 잉크 특성에 따른 복잡한 거동을 이해하고 실제 잉크젯 공정과 같은 복잡한 유동 환경의 응용을 위한 플랫폼을 마련해 줄 수 있을 것이라고 생각한다.

주요어: 압전 잉크젯 공정, Z (=Oh^{-1}) 넘버, 링슬릿 장비, 노즐 막힘, 유동에 의한 응집, 전기수력학적 잉크젯 공정, 무차원수, 콘젯, 젯팅 안정성